

Circumstellar shells and mass loss rates: Clues to the evolution of S stars^{*}

A. Jorissen^{1,2**} and G.R. Knapp²

¹ Institut d’Astronomie et d’Astrophysique, Université Libre de Bruxelles, C.P.226, Boulevard du Triomphe, B-1050 Bruxelles, Belgium

² Department of Astrophysical Sciences, Princeton University, Princeton, NJ 08544, U.S.A.

Received date; accepted date

Abstract. It is the purpose of this paper to rediscuss the circumstellar properties of S stars and to put these properties in perspective with our current understanding of the evolutionary status of S stars, in particular the intrinsic/extrinsic dichotomy. This dichotomy states that only Tc-rich (‘intrinsic’) S stars are genuine thermally-pulsing asymptotic giant branch stars, possibly involved in the M–S–C evolutionary sequence. Tc-poor S stars are referred to as ‘extrinsic’ S stars, because they are the cooler analogs of barium stars, and like them, owe their chemical peculiarities to mass transfer across their binary system.

Accordingly, an extensive data set probing the circumstellar environment of S stars (IRAS flux densities, maser emission, CO rotational lines) has been collected and critically evaluated. This data set combines new observations (9 stars have been observed in the CO $J = 2 - 1$ line and 3 in the CO $J = 3 - 2$ line, with four new detections) with existing material (all CO and maser observations of S stars published in the literature). The IRAS flux densities of S stars have been re-evaluated by co-adding the individual scans, in order to better handle the intrinsic variability of these stars in the IRAS bands, and possible contamination by Galactic cirrus.

In the ($K - [12]$, $[25] - [60]$) color-color diagram, S stars segregate into five distinct regions according to their Tc content and ZrO/TiO, C/O and IR spectral indices. Stars with photospheric colors (populating ‘Region A’) may be identified with extrinsic S stars. For the other regions characterized by different excess levels in the 12, 25 and 60 μm bands, several diagnostics (like the IRAS spectral class, maser emission, and shape of CO rotational lines) have been collected to infer the physical properties of the dust shell. A simple radiative-transfer code has also been used

to infer the chemical nature (carbonaceous or silicate) of the dust grains from the observed IR colors. S stars with large $K - [12]$ excesses and moderate $[25] - [60]$ excesses (populating Regions B and C) exhibit the signatures of oxygen-rich shells (9.7 μm silicate emission and SiO maser emission). The situation is less clear for S stars with small $K - [12]$ and moderate $[25] - [60]$ indices (populating Regions D and E). Their IR colors are consistent with carbonaceous grains (as is their featureless IRAS spectrum, and absence of silicate or SiO maser emission), but these features may equally well be explained by a detached shell. For many of these stars with a large 60 μm excess, the shell is indeed resolved by the IRAS beam at 60 μm . The prototypical SC star FU Mon is among these. Since SC stars are believed to be in a very short-lived evolutionary phase where C/O = 1 within 1%, FU Mon may be a good candidate for the ‘interrupted mass-loss’ scenario advocated by Willems & de Jong (1988). The CO line profile of FU Mon is also peculiar in being quite narrow ($V_e = 2.8 \text{ km s}^{-1}$), suggesting that the mass loss has just resumed in this star.

Mass loss rates or upper limits have been derived for all S stars observed in the CO rotational lines, and range from $< 2 \cdot 10^{-8} \text{ M}_{\odot} \text{ y}^{-1}$ for extrinsic S stars to $1 \cdot 10^{-5} \text{ M}_{\odot} \text{ y}^{-1}$ (the Mira S star W Aql). These mass-loss rates correlate well with the $K - [12]$ color index, which probes the dust loss rate, provided that $\dot{M} \gtrsim 10^{-8} \text{ M}_{\odot} \text{ y}^{-1}$. Small mass-loss rates are found for extrinsic S stars, consistent with their not being so evolved (RGB or Early-AGB) as the Tc-rich S stars. This result does not support the claim often made in relation with symbiotic stars that binarity strongly enhances the mass-loss rate.

Key words: Stars: mass-loss – Stars: AGB – Stars: S – Stars: late-type – Infrared: stars – Radio lines: stars

Send offprint requests to: A. Jorissen (at the address in Belgium)

^{*} Based on observations carried out at the Caltech Submillimeter Observatory (Mauna Kea, Hawaii)

^{**} Research Associate, F.N.R.S., Belgium

1. Introduction

The S stars are late-type giants whose spectra resemble those of M giants, with the addition of distinctive molecular bands of ZrO (Merrill 1922). The presence of ZrO bands is often considered as a direct consequence of molecular equilibrium in the special circumstances where the atmospheric C/O ratio is within 10% of unity (e.g. Scalo & Ross 1976). However, Piccirillo (1980) has shown that the above statement is only valid for stars with $T < 3000$ K. At higher temperatures, an enhanced Zr abundance, rather than a C/O ratio close to unity, is the dominant factor in the development of strong ZrO bands. Detailed abundance analyses (Smith & Lambert 1990) have shown that the envelopes of S stars are enriched in heavy elements like Zr, and so bear the signature of the s-process of nucleosynthesis (Käppeler et al. 1989). Although larger than in M giants, the C/O ratio of S stars is not necessarily close to unity (Smith & Lambert 1990), except in the so-called SC stars (Dominy et al. 1986).

When S stars were still believed to be objects with C/O close to unity, they were naturally considered as transition objects between M giants (C/O < 1) and carbon stars (C/O > 1) on the asymptotic giant branch (AGB) (Iben & Renzini 1983). Support to this scenario is provided by observations of S stars on the upper AGB of globular clusters in the Magellanic Clouds (Bessell et al. 1983; Lloyd Evans 1983, 1984, 1985). In this evolutionary phase, low- and intermediate-mass stars are characterized by a double (H, He) burning-shell structure which is thermally unstable. The thermal instabilities (‘thermal pulses’) developing in the He-burning shell are the site of a rich nucleosynthesis (Frost & Lattanzio 1995), probably including the s-process, although its detailed mode of operation remains poorly understood (e.g. Sackmann & Boothroyd 1991; Herwig et al. 1997). In the receding phase of the thermal instability, the convective outer envelope may plunge (‘third dredge-up’) into the intershell zone containing the He-burning ashes, and bring fresh carbon and s-process elements to the surface.

However, several observations have challenged this traditional M–S–C evolution sequence. The first set of observations relates to Tc, an element with no stable isotopes, discovered in the spectra of some S stars by Merrill (1952). If the s-process indeed occurred during recent thermal pulses in S stars, Tc should be observed at the surface along with the other s-process elements (Mathews et al. 1986). Little et al. (1987) found however that only long-period Mira or semiregular S stars (i.e., intrinsically bright S stars) exhibit Tc lines. Second, the broad range of IRAS colors exhibited by S stars (e.g., Jorissen et al. 1993) is difficult to reconcile with the idea that they represent a brief transition phase as the star evolves from an oxygen-rich M giant with C/O < 1 into a C star with C/O > 1. M and C stars occupy well-defined regions in the IRAS color-color diagram, and it is not clear how S stars

fit into the (much debated) evolutionary sequence joining M stars to C stars in that diagram (Willems & de Jong 1986, 1988; Chan & Kwok 1988; Zuckerman & Maddalena 1989; de Jong 1989).

These problems received a new impetus with the discovery that the barium stars, a family of peculiar red giant (PRG) stars of spectral type G and K, are all members of binary systems (McClure et al. 1980; McClure 1983). Iben & Renzini (1983) were the first to propose that Tc-poor S stars could perhaps be the cooler analogs of the barium stars. Long-term radial-velocity monitorings confirmed this suggestion, and it is now clear that Tc-poor S stars are binary stars (Smith & Lambert 1988; Brown et al. 1990; Jorissen & Mayor 1992; Jorissen et al. 1993; Johnson et al. 1993) with orbital elements identical to those of barium stars (Jorissen et al. 1997). Tc-poor S stars are now referred to as ‘extrinsic S stars’, because, like barium stars, they owe their chemical peculiarities to mass transfer across the binary system. On the contrary, Tc-rich, ‘intrinsic S stars’ are genuine thermally-pulsing (TP) stars on the TP-AGB. Since the C/O ratio of extrinsic S stars depends on the details of the mass accretion process, it is not necessarily close to unity, but as discussed above, neither abundance analyses nor predictions of molecular chemical equilibrium really require C/O to be close to unity in S stars.

In Paper I (Jorissen et al. 1993; see also Groenewegen 1993), it was shown that the correlation Tc-poor/binary found for S stars could be extended to their IRAS colors, since another distinctive property of binary, Tc-poor S stars is the absence of IR excesses. Their IRAS colors simply reflect the photospheric colors, contrary to Tc-rich S stars which usually exhibit IR excesses. These IR excesses are caused by circumstellar dust, and are indicative of substantial mass loss, thus suggesting that Tc-rich S stars are more massive and/or more evolved than Tc-poor S stars.

The possibility offered by the circumstellar properties of S stars to probe their evolutionary status has been used in several recent studies (Jura 1988; Chen & Kwok 1993; Bieging & Latter 1994; Sahai & Liechti 1995). However, these studies still rely on hypotheses not fully consistent with the dichotomy recently found among S stars, as discussed above, and their conclusions may therefore be somewhat biased. For example, it makes no sense to test the AGB evolutionary sequence M–S–C using a sample of S stars not properly cleaned from its extrinsic content. In addition, models inferring the chemical nature (carbonaceous or silicate) of the dust grains from models assuming that C/O is close to unity in the photosphere do not sample the whole parameter space occupied by these stars. A similarly incorrect corollary consists of concluding that dust production, and thus mass loss, is not very efficient in S stars because dust-seed molecules no longer form in the absence of any free C or O atoms, since these are all tied up in CO when C/O \sim 1.

It is the purpose of this paper to rediscuss the circumstellar properties of S stars and to put these properties in perspective with our current understanding of the evolutionary status of S stars, in particular the intrinsic/extrinsic dichotomy. An extensive data set probing the circumstellar environment of S stars (IRAS colors, maser emission, CO rotational lines) has therefore been collected and critically evaluated. This data set combines new material with existing results collected from the literature.

The IRAS colors of S stars provide a first way to probe their circumstellar environment, and more specifically, to evaluate the amount and nature of the dust surrounding these objects. A re-evaluation of the flux densities listed in the IRAS *Point Source Catalogue* (IRAS Science Team 1988; PSC) was necessary to circumvent the problems of interpretation related to the intrinsic IR variability of these sources and to their possible contamination by Galactic cirrus emission. These effects are not always properly handled in the PSC. This re-evaluation was performed by co-adding the raw scans (Sect. 2.2). The clean flux densities were then used to define five regions in the $(K - [12], [25] - [60])$ color-color diagram (Sect. 2.3) which contain stars of similar extrinsic or intrinsic nature and of similar ZrO/TiO, C/O and IR spectral indices. Several S stars with shells resolved at 60 (and sometimes 100) μm have been found by comparing the source profile with the IRAS point source response function (Sect. 2.4). Resolved shells at 60 μm appear to be correlated with large 60 μm excesses, suggesting that these shells have detached from their parent star. A simple model of the dust shell has been used to predict its IR colors and to infer the chemical nature of the dust grains (Sect. 4), using constraints provided by the detection or non-detection of maser emission (Sect. 3). Finally, mass loss rates have been derived in an homogeneous way (Sect. 5.3) from the intensities of the CO millimeter-wave lines, derived from new observations with the Caltech Submillimeter Observatory (Sect. 5.1) or collected from the literature (Sect. 5.2). The mass loss rates, wind expansion velocities, IR colors and extrinsic/intrinsic nature are then discussed together in Sect. 6.

2. Infrared colors of S stars

2.1. The sample

The sample of S stars considered in this paper was selected from the list of Chen et al. (1995), which provides associations between IRAS sources from the PSC and S stars from the *General Catalogue of Galactic S Stars* (GCGSS, Stephenson 1984) and from an additional later list (Stephenson 1990). Among these, only stars having flux densities of good quality (i.e. with a quality flag of 3 in the PSC) in the 12, 25 and 60 μm bands have been retained.

Several stars that have probably been misclassified as S stars were removed from the final sample. For example, stars from the original Westerlund & Olander (1978) sample were later recognized by Lloyd Evans & Catchpole (1989) as actually being heavily-reddened M giants or supergiants. A few other cases of M giants or supergiants misclassified as S stars were identified by Keenan & McNeil (1989; HR 3296 = GCGSS 500) and Winfrey et al. (1994; GCGSS 1314 and star 41 in Stephenson 1990). A detailed heavy-element abundance analysis (Lambert et al. 1995) has shown that the stars DE Leo (HR 4088) and HR 7442, although often considered as S stars, have normal abundances. According to Meadows et al. (1987), GCGSS 886 (IRAS 15194-5115) is now classified as a carbon star and thus has not been retained in the final sample of S stars. Our final sample may still be somewhat contaminated by M supergiants misclassified as S stars and by a few carbon stars. The star T Cet for example was classified as M5-6Se in the original paper by Keenan (1954) defining the S class, but it was reclassified as M5/M6Ib/II in the Michigan Spectral Survey (Houk & Cowley 1975). Since at the low plate dispersions used in classification work, these two types of spectra look similar (e.g. Lloyd Evans & Catchpole 1989), T Cet has been kept in our final list until higher resolution spectra resolve these conflicting classifications. The same holds true for TV Dra and OP Her (see Table 2 of GCGSS). Note, however, that SC stars like RZ Peg, FU Mon and GP Ori are retained in the sample, since they may provide important clues to the evolutionary status of S stars as a whole. Similarly interesting are the two CS stars TT Cen and BH Cru that are known to exhibit ZrO bands at some times and C₂ bands at others (Stephenson 1973; Lloyd Evans 1985).

2.2. The IRAS flux densities

The final sample consists of 124 S stars having flux densities at 12, 25 and 60 μm flagged as being of good quality in the PSC. These stars are listed in Table 1. However, PSC flux densities suffer from several shortcomings that make them inadequate for the present study. First, the 60 μm flux density may in some cases be seriously contaminated by Galactic cirrus emission, as shown by Ivezić & Elitzur (1995). Second, the PSC flux densities are not appropriate in the case of slightly extended or variable sources, as several S stars appear to be. Moreover, hysteresis of the detectors hampers the search for extended sources and should be properly identified. Finally, the detectors may saturate on very bright sources, those with flux densities in excess of 1000 Jy (like χ Cyg, see Appendix A).

In order to correctly handle these effects, the raw IRAS data for all S stars in our sample were reprocessed through the ADDSCAN procedure provided by the *Infrared Processing and Analysis Center* (IPAC¹). This pro-

¹ IPAC is operated by the *Jet Propulsion Laboratory* and *California Institute of Technology* for NASA

cedure has been used to co-add all scans passing within $1.7'$ of the target position. Before being co-added, the raw data are first interpolated using cubic splines and re-sampled at 10 data points per arcminute in all bands. A baseline is then defined for each individual scan by fitting a parabola to the data in a window extending from r_{in} to r_{out} from the target ($r_{\text{in}} = \pm 2', \pm 2', \pm 2.5', \pm 4'$ and $r_{\text{out}} = \pm 7.5', \pm 7.5', \pm 10', \pm 13.5'$ in the 12, 25, 60 and $100 \mu\text{m}$ bands, respectively). The r.m.s. residual σ_i of the data around the baseline fit is an indication of the background noise in a given scan i (note that possible nearby sources with a peak flux density exceeding $2.5\sigma_i$ are automatically removed and do not enter the final residual calculation). The different scans are then co-added with weighting factors equal to $1/\sigma_i^2$. The noise σ in the co-added scan, computed in a similar way as for the individual scans, is smaller than that in any individual scan, and the reduction may be substantial when scans with very different orientations, sampling different regions of the sky around the target, are available, since structure in the Galactic cirrus emission contributes to the noise. Finally, a point-source template with adjustable width is fitted to the co-added scan in the target window $\pm r_{\text{in}}$. Three different estimates of the flux densities in each band are then computed: the peak flux density F_p , the template flux density F_t and the ‘zero-crossing’ flux density F_z . The template flux density F_t is derived from the template fit to the data, and generally agrees with F_p , unless the source is extended or hysteresis effects are important. For extended sources, the ‘zero-crossing’ flux density F_z must be preferred. It corresponds to the integrated flux density between the ‘zero crossings’, which are defined as the first locations, moving outwards from the peak location, where the source profile intersects the baseline. In Sect. 2.4, a criterion based on the comparison of F_z and F_p has been designed to identify sources with possibly resolved shells. If that criterion is met, the F_z flux density (identified by a ‘+’ in Table 1) has been adopted instead of F_t . In the case of bright sources, detector hysteresis results in a trail extending along the scan direction, thus disturbing the template fit. In that case, F_p has been adopted. The template fit to sources embedded in strong Galactic cirrus emission generally resulted in an abnormally narrow profile, because the adopted baseline is then too high with respect to the base of the source signal. These contaminated sources were thus readily identified by their narrow profile, and were rejected. Finally, individual scans clearly contaminated by nearby sources have been eliminated.

The adopted IRAS flux densities are listed in Table 1 in columns 5–8. The $2.2 \mu\text{m}$ flux density is listed in column 3. The calibration of Beckwith et al. (1976; 620 Jy corresponds to $K = 0$) has been used to derive the $2.2 \mu\text{m}$ flux density from the K magnitude provided by different authors, as listed in column 4: 1: Catchpole et al. (1979); 2: Neugebauer & Leighton (1969; *Two-Micron Sky Sur-*

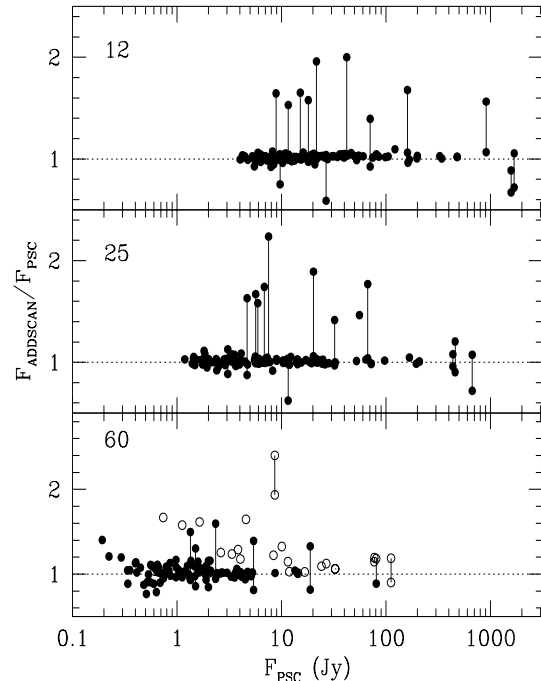


Fig. 1. Comparison between the PSC flux densities and those derived from the ADDSCAN procedure (see text) in the 12, 25 and $60 \mu\text{m}$ bands. Flux densities of variable sources at two different epochs are connected by a vertical line. At $60 \mu\text{m}$, open circles correspond to extended sources (see Sect. 2.4)

vey); 3: Mendoza & Johnson (1965); 4: Price (1968); 5: Chen et al. (1988); 6: Noguchi et al. (1991); 7: Guglielmo et al. (1993); 8: Epchtein et al. (1990); 9: Epchtein et al. (1987); 10: Lloyd Evans & Catchpole (1989).

The Tc content (from Paper I, and Lambert et al. 1995) is listed in column 9. The columns labelled ‘LRS’ and ‘VC’ provide the classification of the IRAS low-resolution spectrum, according to the IRAS *Low Resolution Spectrometer Catalogue* (Olson et al. 1986) or to the Volk & Cohen (1989) schemes, respectively. The optical spectral type is from the GCGSS. The variability type, the period and the range of variation of the magnitude (lowest minimum - highest maximum) are from the *General Catalogue of Variable Stars* (Kholopov et al. 1985; GCVS). The variable name and/or the HD/HR designations, when available, are given in the last column. If maser emission has been detected (see Sect. 3 and Table 3), the maser type (SiO or OH) is given between parentheses after the stellar designation.

Several sources observed by IRAS a few months apart turn out to be strongly variable in the IRAS bands. For these, the ADDSCAN procedure has been run separately on the two groups of data, and the flux densities are listed on two separate lines in Table 1. The corresponding approximate Julian dates have been derived from the ‘Satellite Operation Plan’ number attached to the scans and

from the mission chronology provided in Table III.C.1 of the IRAS *Explanatory Supplement* (1988).

The flux densities derived from the ADDSCAN procedure generally agree with the PSC flux densities within 20%, as shown in Fig. 1. In all bands, the scatter is larger at low flux densities. Several stars show much larger deviations because of intrinsic variability. For these, it turns out that the PSC flux densities correspond to one epoch, whereas the flux densities at the other epoch may differ by as much as a factor of 2. An example of a strongly variable source, χ Cyg, is discussed in Appendix A. In the 60 μm band, large discrepancies are also found for extended sources, as expected (see Sect. 2.4).

2.3. The infrared color-color diagrams

The use of the $([12] - [25], [25] - [60])$ diagram to probe the circumstellar shells surrounding late-type stars was first demonstrated by Hacking et al. (1985) and by van der Veen & Habing (1988, VH). VH defined various regions (labelled I to VII) corresponding to circumstellar shells with relatively homogeneous properties. Figure 2 presents the $([12] - [25], [25] - [60])$ diagram for the sample of S stars defined in Sect. 2.1. In this paper, the color index $[i] - [j]$ is defined as $[i] - [j] = -2.5 \log[(F(i)/F_0(i))/(F(j)/F_0(j))]$ (where $F(i)$ refers to the non-color corrected flux density in the IRAS band i , and $F_0(i)$ is a normalization flux density as given in the IRAS *Explanatory Supplement* 1988). With this normalization, black bodies in the Rayleigh-Jeans limit have a color index of 0. The colors for stars whose IRAS flux densities show large variations are plotted as two symbols joined by a line segment.

There is a strong correlation between the position of an S star in the color-color diagram and the intensity of the spectral features distinctive of the S star class (as measured by the ZrO/TiO or C/O spectral indices in the spectral classification schemes devised by Keenan 1954 and Keenan & Boeshaar 1980, respectively; both will be called ‘ZrO index’ for simplicity in the following). In particular, S stars with ZrO indices larger than 3 are mainly found in Regions VII and VIa with a few more in Region III, while S stars with ZrO indices smaller than or equal to 2 are found mainly in Regions I and II. This segregation of S stars in the $([12] - [25], [25] - [60])$ diagram is a clear indication of the inhomogeneous nature of this family of peculiar red giants. In the center of Region I lie the S stars with photospheric colors. These are in fact the binary and Tc-poor S stars (‘extrinsic’ S stars) that owe their chemical peculiarities to mass transfer in a binary system (Sect. 1). Another group of weak S stars is found at the boundary between Regions I and II, a zone generally devoid of stars in the $([12] - [25], [25] - [60])$ diagram (see e.g. VH, and Lewis 1989). This group includes the prototypical Tc-rich Mira S variable χ Cyg. The few S stars located in Region II, defined by VH as comprising O-rich stars with ‘young’

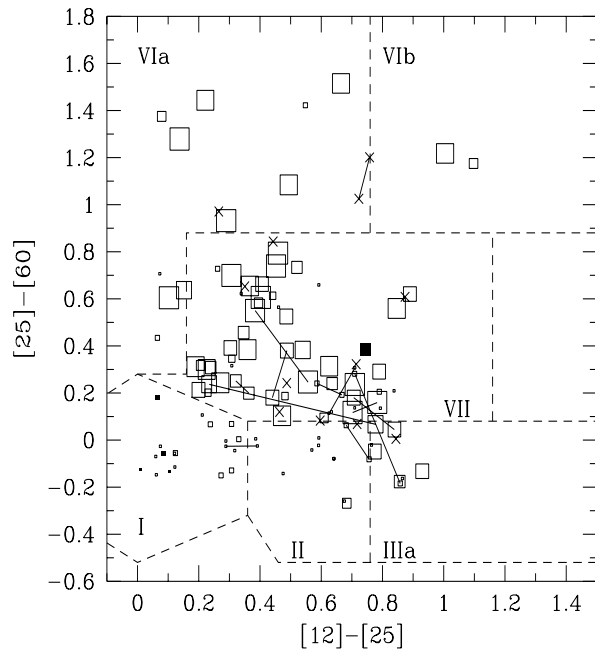


Fig. 2. The $([12] - [25], [25] - [60])$ diagram for S stars. The size of the square is proportional to the ZrO/TiO or C/O spectral index of the S star (whichever is available), in the spectral classification scheme of Keenan (1954) or Keenan & Boeshaar (1980), respectively. MS and SC stars were assigned classes 1 and 9, respectively. Crosses correspond to stars with no spectral type available in the GCGSS. Tc-poor S stars are represented by filled squares, and colors of variable stars measured at different epochs are connected by a line segment

circumstellar shells, indeed have small ZrO indices. Most S stars populate Region VII, where C-rich circumstellar shells are found according to VH, and it is therefore not surprising that those S stars have large ZrO indices. Finally, several stars (among which are many of type SC) are located in Regions VIa and b, many of them having conspicuously resolved circumstellar shells (see Sect. 2.4).

Several authors (see e.g. Habing 1996) have argued that the $K - [12]$ index is superior to the $[12] - [25]$ index for tracing the mass loss rate, the focus of the present study, because of its greater wavelength range and the fact that the photosphere emits more strongly at K while the shell emits more strongly at 12 μm . Therefore, we felt that it was more meaningful to use the $(K - [12], [25] - [60])$ diagram to define groups of S stars with homogeneous IR properties, as follows (Fig. 3):

- Region A: S stars with photospheric IR colors (‘extrinsic S stars’);
- Region B: S stars with no excesses at 60 μm , and small ZrO indices;
- Region C: S stars with excesses in all three 12 μm , 25 μm and 60 μm bands, and large ZrO indices;
- Region D: S stars with large ZrO indices and 60 μm excesses, but small 12 μm excesses;

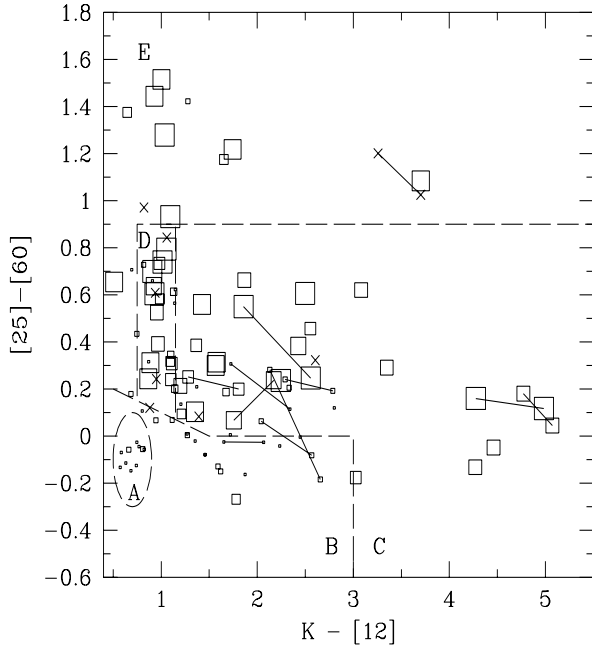


Fig. 3. Same as Fig. 2 for the $(K - [12], [25] - [60])$ diagram. Note that the $K - [12]$ index may be inaccurate for variable stars, since their K and $[12]$ magnitudes were not measured simultaneously

Region E: mainly SC stars with large $60 \mu\text{m}$ excesses and often resolved shells.

The stars classified this way are plotted in the $([12] - [25], [25] - [60])$ color-color diagram in Fig. 4, and it is seen that the above regions almost exactly correspond to those of VH, with the exception of Region B which encompasses both Regions I and II, and Region VII which is a blend of Regions C and D (though stars from Region D are concentrated in the upper left of Region VII). The motivation for creating Region D is apparent in Fig. 5, which presents the distribution of the various IR spectral types (as defined by Volk & Cohen 1989) across the $(K - [12], [25] - [60])$ diagram. Region D differs from Region C in having many stars exhibiting a stellar continuum in the IR (class S) and none with silicate emission (class E). As it will be shown in Sect. 4, these features suggest that the circumstellar shells in Region D contain C-rich grains, whereas silicate grains are found in the circumstellar shells of Region C. Note that Regions C and D are also quite distinct in the $(K - [12], [12] - [100])$ diagram (Fig. 6).

Finally, let us remark that the different regions defined above have been denoted by uppercase letters to avoid confusion with the Regions a to d defined in Paper I from the lower-accuracy PSC flux densities. The new classification into Regions A–E is actually not very different from that in Paper I (matching uppercase with lowercase letters, and with Region d splitting into D and E), but it is clearly superior since several stars that appeared excep-

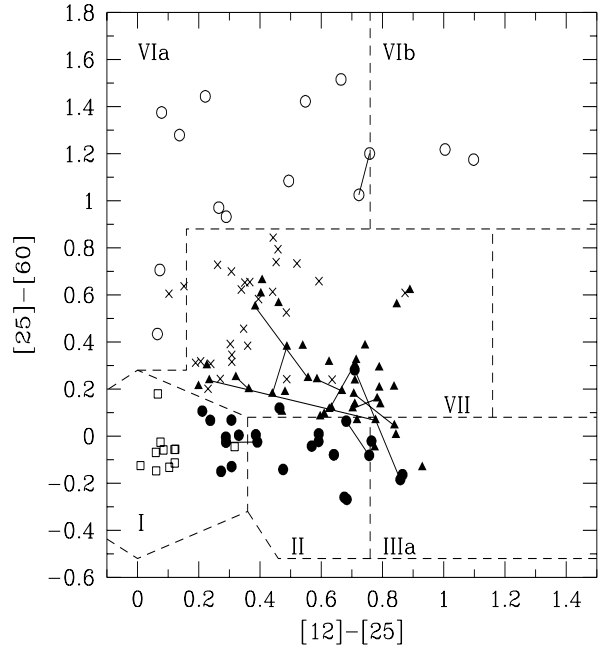


Fig. 4. Same as Fig. 2, where the stars have been drawn with a symbol corresponding to the region they belong to in the $(K - [12], [25] - [60])$ diagram (Fig. 3), as follows: open squares: Region A; filled circles: Region B; filled triangles: Region C; crosses: Region D; open circles: Region E

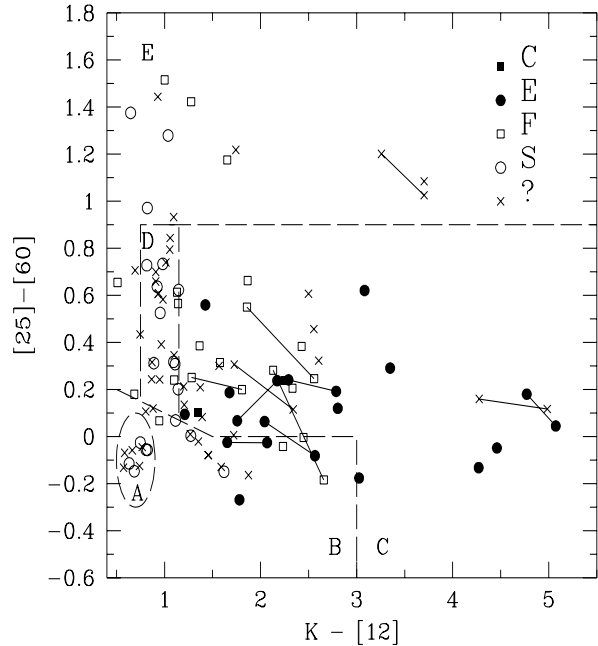


Fig. 5. Same as Fig. 3, with symbols referring to the spectral class of the IRAS low-resolution spectrum as defined by Volk & Cohen (1989): S: stellar continuum; F: featureless spectrum; E: silicate emission; C: SiC emission; ?: not available. Spectral type assignments for S stars are from Chen et al. (1995)

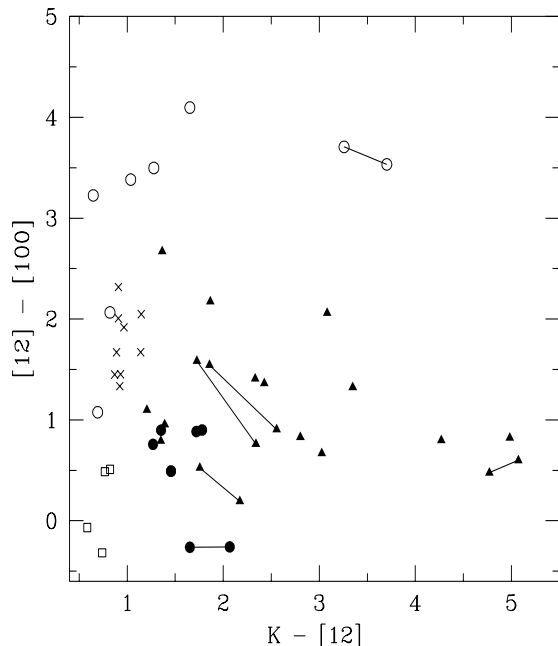


Fig. 6. The $(K - [12], [12] - [100])$ diagram. Symbols are as in Fig. 4

tional in Paper I fit well into the present classification. For instance, χ Cyg, NQ Pup and o^1 Ori were exceptional as being Tc-rich stars in Region a. With the more accurate ADDSCAN flux densities, χ Cyg moves to Region B (see also Appendix A) while NQ Pup and o^1 Ori move to Region E. The only remaining outliers in this respect are HR Peg, the only Tc-rich star in Region A, and DY Gem, the only Tc-poor star not in Region A (but in C). DY Gem is however exceptional in many other respects: it is a very cool star (S8,5 corresponding to $T_{\text{eff}} = 3000$ K; Smith & Lambert 1990) and a SRa variable with a very long period (1145 d). Moreover, it has the largest $[12] - [100]$ index among stars in Region C (see Fig. 6).

2.4. S stars with envelopes resolved at $60 \mu\text{m}$

The possibility that some S stars may have circumstellar shells resolved by IRAS is now examined. As argued by Young et al. (1993a; YPK), the $60 \mu\text{m}$ band is best suited for that purpose, because it is not contaminated by Galactic cirrus emission as severely as is the $100 \mu\text{m}$ band. The $60 \mu\text{m}$ co-added scans were examined, and characterized as follows. First, the width of the template profile fitted to the source is compared to that expected for point sources, namely $2'.05$ and $1'.44$ full widths at the 25% and 50% levels, respectively (Levine et al. 1993). However, this criterion is not sensitive to resolved shells showing up as a weak plateau at the base of the profile. A simple criterion has therefore been devised, based on the comparison of the ‘peak flux density’ F_p with the ‘zero-crossing

flux density’ F_z (see Sect. 2.2). These quantities are standard outputs from the ADDSCAN procedure. In the case of a point source, F_z and F_p are identical within a few times the noise, measured as the rms σ of the residuals along the baseline outside the signal range (i.e. between $2'.5$ and $10'$ from the target position in either directions) after baseline subtraction (see Sect. 2.2). In the case of an extended source, the fraction ϵ of flux density in excess of that of a point source is expressed by $\epsilon = (F_z - F_p)/F_p$. For estimating the significance of this excess, one has to be aware of the following effects. First, very bright (> 500 Jy) sources may have a characteristic six-pointed star shape due to reflection from the telescope secondary mirror struts. Since approximately 5% of the peak flux density may be contained in the star pattern, F_z/F_p values of the order of 1.05 may be of instrumental origin (Levine et al. 1993). Bright sources are also affected by hysteresis in the detector which causes a trail in the signal along the scan direction in the outgoing part of the scan. This trail is easily recognized on individual scans as it causes an asymmetry in the template fit. However, if the co-added scan results from individual scans made in opposite directions, as is often the case, trails will be present in both directions and will mimick an extended plateau at the base of the profile. For bright sources (> 100 Jy), this effect may thus also cause spurious excesses of the order of a few percent. Finally, for fainter sources, an inhomogeneous background may also cause spurious detections. In this case, a way to estimate the significance of the excess ϵ is to compare it with the inverse signal-to-noise ratio $1/SNR = \sigma/F_p$, which is nothing more than the relative flux density excess expected from the background noise. The significance, or ‘quality factor’ QF , of the observed flux density excess can then be expressed as $QF \equiv \epsilon F_p/\sigma = \epsilon SNR$, so that $QF > 5$ for a detection at the 5σ level. Figure 7 presents the ratio F_z/F_p vs SNR for S stars not confused by nearby sources, and several stars with $QF > 5$ are found. One has to be aware, however, that the co-addition process will be mostly effective in lowering the baseline noise far away from the target, where scans with different orientations sample different regions of the sky. But since they all intersect approximately on the target, the noise-averaging process will not be as effective on the target. A criterion based on the absolute noise level present on-target has therefore been considered as well, by requiring that, to be considered significant, an excess $F_z - F_p$ should not be smaller than some given threshold value of the order of the background fluctuations in the $60 \mu\text{m}$ band. It was found that meaningful results are obtained by adopting 0.3 Jy as the typical background fluctuation on-target, combined with a quality factor of 5. In Fig. 7, sources satisfying the $F_z - F_p > 0.3$ Jy criterion have been represented by open squares. Since very few square symbols are located below the dashed line in Fig. 7, both criteria are fulfilled simultaneously for most of the stars, and thus provide consistent conclusions regarding the resolved nature of these sources.

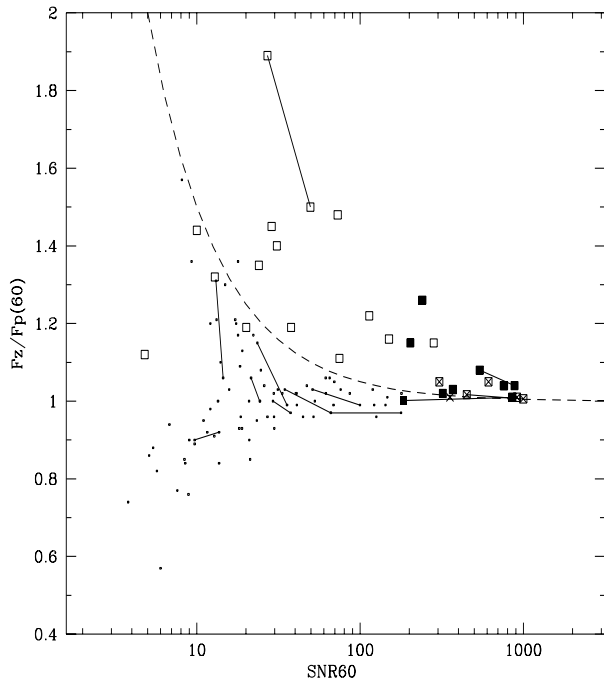


Fig. 7. The ratio F_z/F_p between the ‘zero-crossing flux density’ and the ‘peak flux density’ in the $60\ \mu\text{m}$ band, vs the S/N ratio along the baseline (see text for details). Stars lying above the dashed line have a flux density excess in the $60\ \mu\text{m}$ band with a quality factor larger than 5. Stars with a flux density excess above the $0.3\ \text{Jy}$ threshold are represented by squares. Squares lying above the dashed line thus satisfy both criteria defined in the text and are probably truly resolved sources. Filled squares and crosses correspond to sources flagged by YPK as extended or non-extended, respectively, at $60\ \mu\text{m}$. Observations of the same star at two different epochs are connected by a line segment. Sources confused with a nearby source are not plotted

Sources flagged as extended at $60\ \mu\text{m}$ by the above criteria are listed in Table 2. Columns 1, 2 and 3 give the IRAS name, the variable star name and variability type when available, respectively. The zero-crossing flux density F_z is in column 4. Column 5 lists the flux density ratio F_z/F_p , and columns 6 and 7 the full widths W_{25} and W_{50} at the 25% and 50% levels, respectively, to be compared with $2'.05$ and $1'.44$ for a point source (Levine et al. 1993). The quality factor QF is listed in column 8. Mass loss rates and wind terminal velocities are given in columns 9 and 10 (see Sect. 5).

A similar search for late-type giants with resolved shells was performed by Young et al. (1993a,b). These authors used a more sophisticated method based on the possibility of successfully fitting the signal by a point source surrounded by a circumstellar shell having ‘reasonable’ properties. Our simpler approach has the advantage of being applicable to fainter stars, and several have indeed been detected, as seen in Fig. 8. However, for bright sources, our method is more vulnerable to spurious de-

tections due to hysteresis (YPK used only the scan data taken *prior* to passing over the source).

As can be seen in Table 2 (in column 11, YPK+ and YPK- denote sources flagged by YPK as extended or not at $60\ \mu\text{m}$, respectively), the two methods give conflicting results for four stars, R And, S Cas, W Aql and T Cet among the 11 bright objects common to the two samples. In the first three cases, our detection is probably an artefact due to detector hysteresis, since *individual* (as opposed to co-added) scans show an extended tail only on the side posterior to the passage over the source (see Fig. 10 below). The situation is less clear for T Cet, as its $100\ \mu\text{m}$ profile is wider than the point-source template, suggesting that this source may be truly extended.

Figure 8 presents the flux density excess F_z/F_p vs $F(2.2)$, the flux density at $2.2\ \mu\text{m}$, and reveals that the properties of the resolved shells in Regions B and C are very different from those of Regions D and E. In Regions B and C, the flux density excess is of the order of a few percent, with a maximum of 15% for Y Lyn. Because the flux density excess is so small, the envelopes around stars in Regions B and C can be resolved only for the stars closest to the sun [i.e. with large $F(2.2)$], as shown by Fig. 8. By contrast, stars in Regions D and E have much larger flux density excesses at $60\ \mu\text{m}$, which make them detectable at much lower total flux density levels. Stars in Regions B and C also differ markedly from those in Regions D and E as far as the $[60] - [100]$ index is concerned (Fig. 9; see also Fig. 6): the resolved envelopes in Regions D and E go along with large $100\ \mu\text{m}$ excesses, suggestive of cool dust in detached envelopes, contrary to the situation prevailing in Regions B and C (the only exception being T Sgr, which appears as a border case between C and D). In the case of RZ Sgr, which is extended in both the $60\ \mu\text{m}$ (YPK) and $100\ \mu\text{m}$ bands (according to the IRAS *Small Scale Structure Catalogue* 1985), an optical nebula has even been reported by Whitelock (1994).

In Region E, $\sigma^1\ \text{Ori}$ and S929 do not follow the general trend. In those cases, there may be a confusing background source responsible for the strongly asymmetric $60\ \mu\text{m}$ profile (see Fig. 10), as the $100\ \mu\text{m}$ profile is offset by about $1'$ in the direction of the $60\ \mu\text{m}$ asymmetry. The extension observed for S929 may be real; its $[60] - [100]$ color index changed by only 2% between the two IRAS observations, while the $60\ \mu\text{m}$ flux density changed by 20%. This color stability is observed in other variable IRAS sources like $\chi\ \text{Cyg}$ (see Appendix A), but would probably not be preserved if the excess flux density were due to a background source.

Finally, the flux density excess in Regions D and E is associated with a widening of the whole $60\ \mu\text{m}$ (and sometimes $100\ \mu\text{m}$) source profile, whereas the excess for stars in Regions B and C is caused by a weak plateau at the base of the profile, as apparent on Fig. 10. For the resolved shells in Regions D and E, the full widths at the 25% and 50% flux density levels (Table 2) are indeed much larger

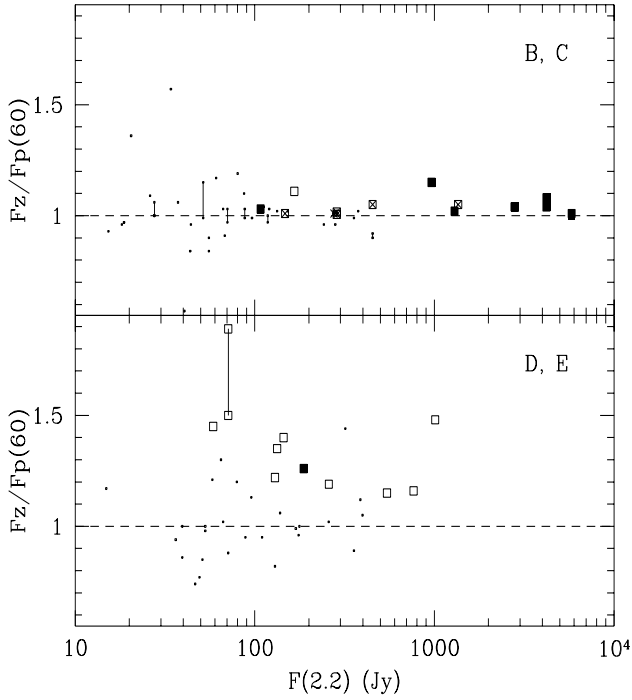


Fig. 8. Flux ratio F_z/F_p vs $F(2.2)$. Symbols are as in Fig. 7, except that large squares now denote stars fulfilling simultaneously our two criteria for extended envelopes. Stars have been separated according to Regions B, C (upper panel) and D, E (lower panel)

than those expected for a point source. HD 191630 and RZ Sgr are listed in the IRAS *Small Scale Structure Catalogue* as extended at 60 μm and 100 μm , respectively. In fact, this distinctive feature of the resolved shells in Regions D and E has been used to include in Table 2 two stars (BI And and AA Cam) with wide profiles, despite quality factors $QF < 5$ that would normally not qualify them. However, these are distant stars with small 60 μm flux densities, so that the F_z/F_p ratio cannot be determined accurately (and is therefore not listed in Table 2).

Stars with resolved shells are represented as black dots in the $(K - [12], [25] - [60])$ diagram (Fig. 11). This figure illustrates the relative contribution of the extended shell to the $[25] - [60]$ index: a line segment joins the $[25] - [60]$ indices computed from the ‘zero-crossing’ flux density F_z at 60 μm (measuring the combined contributions of the star and its resolved shell) and from the ‘template’ flux density F_t , which is assumed to be a rough measure of the stellar contribution alone (represented by a black dot in Fig. 11). Although that assumption is certainly a very rough one, it is not totally unreasonable as stars from Region E now move down, and most reach Regions B, C and D when adopting F_t instead of F_z to represent the 60 μm photospheric flux density. Some stars, however, do not quite leave Region E, presumably because the point source fitting yielding F_t does not entirely remove the contribution of the resolved shell in those cases.

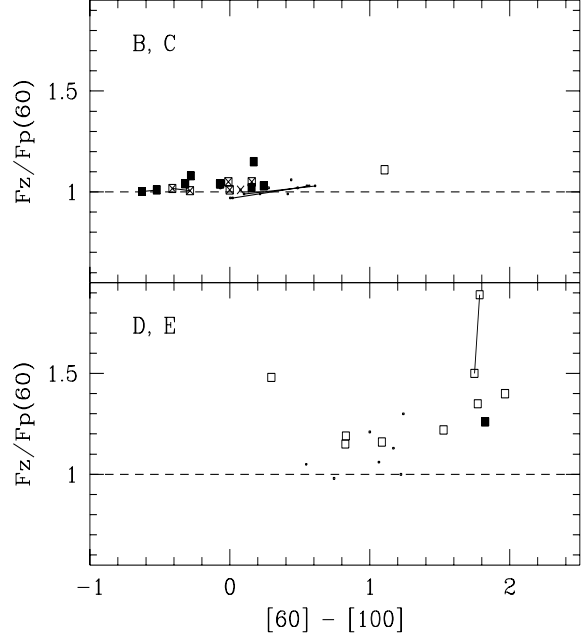


Fig. 9. Same as Fig. 8 for F_z/F_p vs $[60] - [100]$

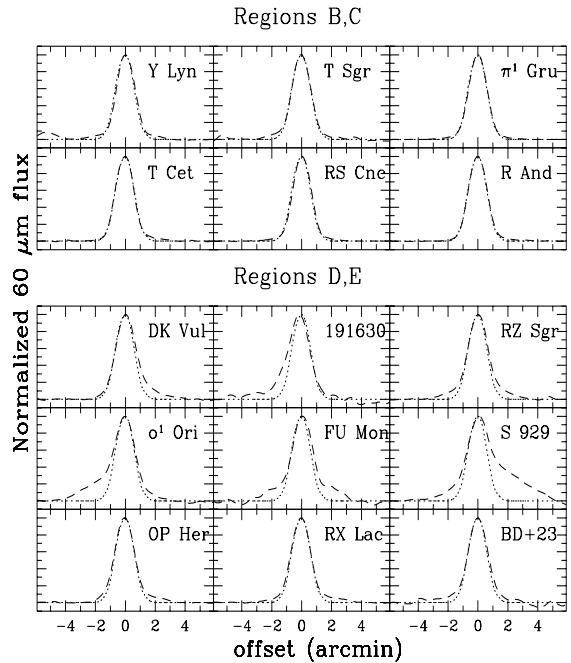


Fig. 10. The 60 μm co-added, spline-interpolated scans (dashed lines) for all stars with a possibly resolved shell in Regions D – E, and for selected cases in Regions B – C (see Table 2). The dotted line is the template 60 μm profile as provided by IPAC. Note how larger the deviations from the template are in Regions D – E as compared to Regions B – C. In the latter case, the deviation of the observed profile from the template profile is due to a weak extended tail. Such detections are therefore vulnerable to detector hysteresis (see text)

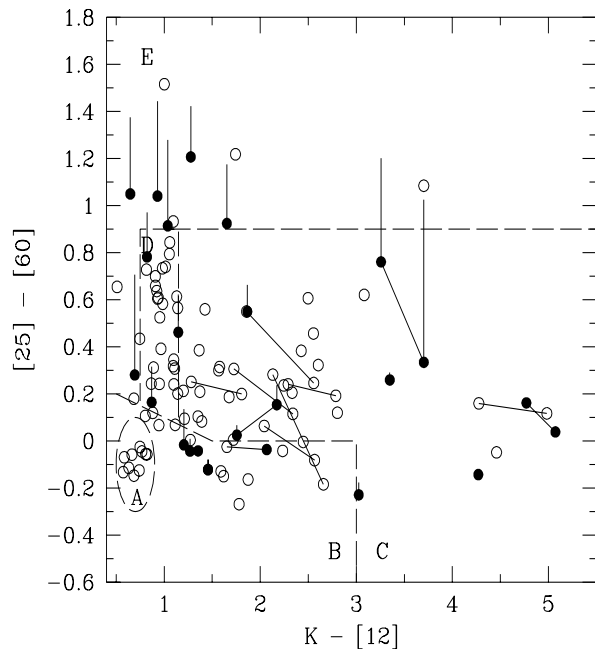


Fig. 11. Position of the sources with resolved shells (filled circles) in the the $(K - [12], [25] - [60])$ diagram. The filled circles represent the color computed from the ‘template’ flux density F_t at $60 \mu\text{m}$, i.e. they roughly correspond to the flux density of the star alone. The upper end of the vertical segment is located at the color computed from the ‘zero-crossing’ flux density F_z at $60 \mu\text{m}$, i.e. the shell + star color

Especially interesting is the fact that Y Lyn and OP Her move from Regions C and D, respectively, to Region B, which is well in line with their small ZrO index (see Fig. 3 where they appear as outliers). With this adjustment, all three SRc variables in our sample (RS Cnc, Y Lyn and T Cet) now belong to Region B, and moreover have resolved shells (tentative in the case of T Cet). As noted by Young et al. (1993a,b) and Habing (1996), resolved shells are a common property of semi-regular variable stars.

Finally, it should be mentioned that several of the stars with a shell resolved by IRAS turn out to have an extended CO shell as well, as derived in Sect. 5.3 from the modelling of the CO data. The inferred radius of the CO shell (Table 6) is larger than $10''$ for χ Cyg ($18''$), W Aql ($23''$), π^1 Gru ($15''$) and FU Mon ($60''$).

3. Masers in S stars

This section presents data collected from the literature on SiO, OH or H₂O maser emission from S stars (relying on the compilation of Benson et al. 1990 for the earlier literature). These data are summarized in Table 3. The detection of SiO, OH or H₂O maser emission is a clear indication that the circumstellar shell is oxygen-rich (see e.g. Deguchi et al. 1989, Lewis 1996), thus providing an

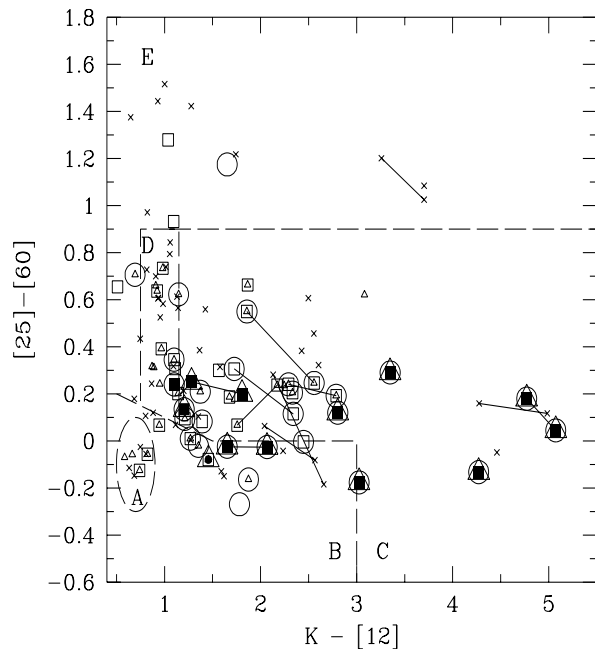


Fig. 12. Location of the maser sources in the $(K - [12], [25] - [60])$ diagram. Positive detections correspond to filled symbols, non-detections to open symbols, and stars not probed for maser emission to crosses. Squares stand for SiO masers, triangles for H₂O masers and circles for OH masers

important constraint on the chemical nature of the dust grains (see Sect. 4). In Table 3, ‘Y’ or ‘N’ in the SiO, OH or H₂O columns means that the corresponding maser is or is not present, respectively, whereas a dash indicates that the maser has not been searched for in a given star.

The masers which are found in S stars are mainly SiO masers forming in the densest part of the circumstellar envelope near the stellar photosphere. OH maser emission has been detected in RS Cnc by Rudnitskij (1976) but not by Kolena & Pataki (1977), though the latter authors probed a different transition from that (1667 MHz) detected by Rudnitskij (1976).

The S stars with SiO maser emission lie in the lower part of Region C, with some overlap with Regions B and D (Fig. 12). As expected, the region occupied by the masers exactly matches the region delineated by the stars showing the $9.7 \mu\text{m}$ silicate feature in emission (IRAS LRS class E; Fig. 5). Indeed, 6 of the 8 SiO masers with an available LRS class are of class E, the only exceptions being R Lyn and EP Vul (class F). On the other hand, no maser emission is observed for stars in Regions D and E (with the exception of EP Vul, but that star lies very close to the boundary with Region C).

4. A simple model of dusty circumstellar shells

4.1. Ingredients of the model

In order to relate the diversity of IR color indices observed among S stars to the underlying physical parameters, synthetic IR color indices of a star embedded in a circumstellar shell have been computed for various input parameters. In our simple model, the star is assumed to radiate as a black body at a temperature T_{eff} . The mass-losing star is surrounded by a spherically-symmetric dust shell extending from r_{in} to r_{out} , with density decreasing as r^{-2} , r being the distance from the central star. This is equivalent to assuming a steady mass-loss rate \dot{M} at constant outflow speed. The inner radius of the dust shell must be larger than or equal to the radius where grains start condensing (i.e., to the radius where the shell temperature drops below 1300 K for silicates, or 1500 K for graphite and amorphous carbon). The shell outer radius is chosen such that $r_{\text{out}}/r_{\text{in}} = 10^4$, which ensures that the color indices of the shell have reached an asymptotic value. A roughly logarithmic radial mesh is defined in the dust envelope so that each shell is optically thin. In each shell, the grains are assumed to be in thermal equilibrium, so that the energy absorbed by the grains exactly balances the energy re-emitted. At the inner boundary, the radiation field is that of a black body of temperature T_{eff} . The model IRAS flux densities are calculated from the emergent spectrum by convolving it with the IRAS filter bandpass (IRAS *Explanatory Supplement*, 1988). The main shortcoming of the code is the neglect of the scattering contribution, since only absorption is taken into account.

Three types of dust grains have been considered: silicates (with a specific mass of 3.5 g cm^{-3}), graphite (with a specific mass of 2.25 g cm^{-3}) and amorphous carbon (with a specific mass of 1.85 g cm^{-3}). The grain radius is $0.2 \mu\text{m}$ in all cases. The absorption coefficients as a function of wavelength are taken from Draine & Lee (1984) and Draine (1985) for silicates and graphite. For amorphous carbon, the absorption coefficients have been generated with the usual Mie formulae using the optical constants provided by Rouleau & Martin (1991). At wavelengths $\lambda > 50 \mu\text{m}$, the spectral index of the emissivity coefficient has been taken equal to -2 for graphite grains, and to -1.5 for amorphous-carbon and silicate grains (Ivezić & Elitzur 1995).

4.2. Synthetic color indices

The results of this model are presented in Fig. 13 for dust shells made of either silicate grains, graphite grains or amorphous carbon grains. Constant *dust* mass loss rates of 10^{-12} , 10^{-10} , 10^{-9} , 10^{-8} and $10^{-7} M_{\odot} \text{ y}^{-1}$ with a wind velocity of 14 km s^{-1} have been adopted. The shell inner radius is set by the grain-condensation temperature, so that the dust shells computed in Fig. 13 are not ‘de-

tached’ (in the sense of Willems & de Jong 1988). The central star has been assigned effective temperatures T_{eff} of 4000 K (solid line) and 3000 K (dashed line), and a luminosity $L = 5000 L_{\odot}$; these parameters turn out to have little impact on the shell colors.

In the $([12] - [25], [25] - [60])$ and $(K - [12], [25] - [60])$ diagrams, the silicate track is quite distinct from the graphite or amorphous-carbon tracks. The graphite and amorphous-carbon tracks go directly from Region I to upper VII (i.e., from A to D and upper C), whereas the silicate track goes from I to II and IIIa (i.e., from A to B and lower C). These differences observed in Fig. 13 between carbon- and oxygen-rich shells must be related to the different emissivities of silicate and carbonaceous grains in the IRAS bands, as discussed by Ivezić & Elitzur (1995).

The tracks for carbonaceous and silicate grains predicted by this simple model outline the segregation observed in the color-color diagrams between S stars with an oxygen-rich shell, as indicated by the $9.7 \mu\text{m}$ silicate feature (IRAS LRS class E), and S stars with featureless IR spectra (IRAS LRS class S – ‘stellar’ – or F – ‘featureless’). It is important to note here that featureless spectra are indeed predicted for carbonaceous grains (Ivezić & Elitzur 1995).

The data on maser emission collected in Sect. 3 are compatible with this segregation. Those S stars which are SiO or OH masers (Table 3) must have an oxygen-rich circumstellar environment, and lie indeed close to the silicate track (Fig. 12). On the contrary, no SiO, OH or H_2O maser emission has been detected for S stars in Regions D and upper C, along the tracks corresponding to carbonaceous grains. Those S stars might therefore possibly be surrounded by C-rich circumstellar shells, especially since they occupy the same region of the color-color diagram as the optical carbon stars (Chan & Kwok 1988).

However, the above picture is not totally satisfactory, since (i) the S stars with silicate emission are actually located *in between* the silicate and carbonaceous tracks, (ii) many stars in Regions D and E have large $60 \mu\text{m}$ excesses that cannot be reproduced by the tracks displayed in Fig. 13, (iii) at least one star (R Gem) moves from the region of silicate dust (lower C) into the region of carbonaceous dust (upper C) during its variability cycle, and (iv) the photosphere of S stars is oxygen-rich, so that their circumstellar shell may be expected to be oxygen-rich as well. The first two mismatches are in fact not specific to S stars, and possible solutions were already suggested by Ivezić & Elitzur (1995). They include either (a) invoking a mixture of silicate and carbonaceous grains (see however the discussion of Sect. 3 on maser emission), (b) decreasing the spectral index of the emissivity at long wavelengths to values smaller than -1.5 , or (c) considering detached envelopes in the sense advocated by Willems & de Jong (1988).

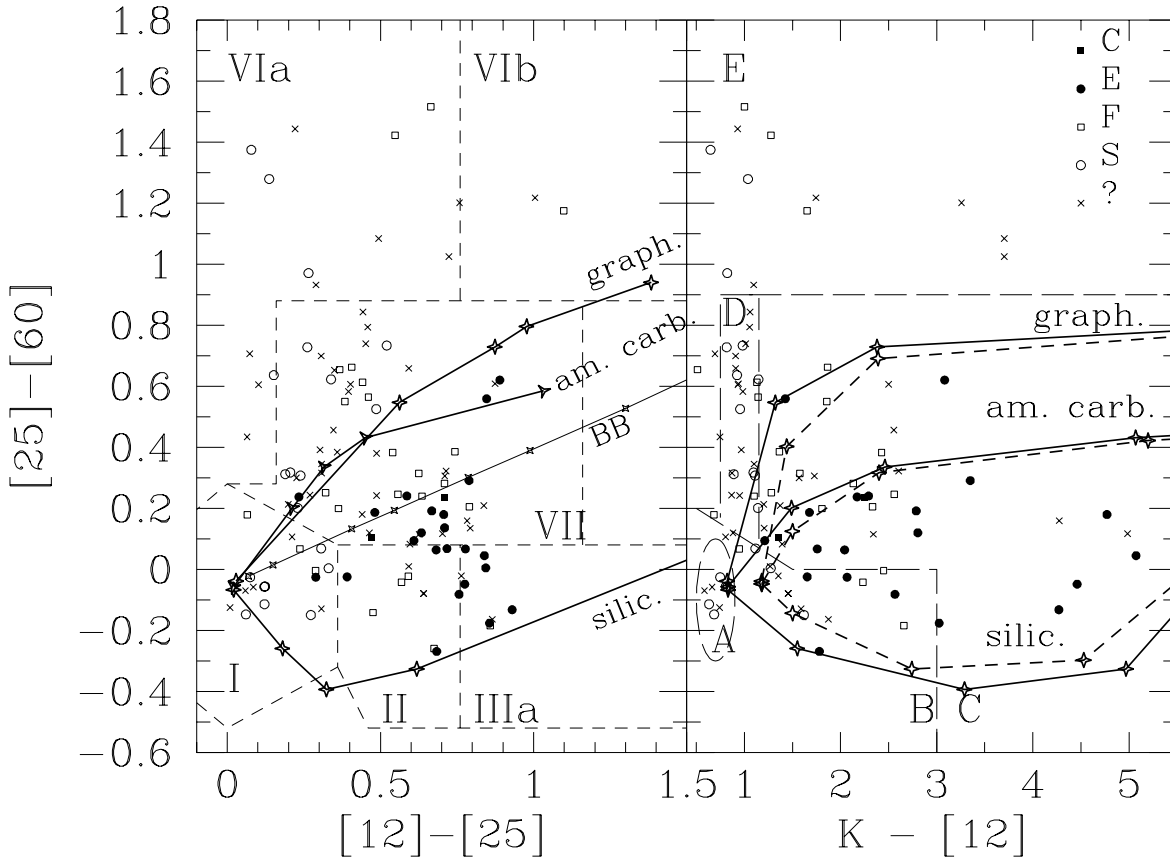


Fig. 13. Left panel: The $([12] - [25], [25] - [60])$ colors predicted for circumstellar shells (with $r_{\text{out}}/r_{\text{in}} = 10^4$) made of silicate grains, graphite grains or amorphous-carbon grains, surrounding a star with $L = 5000 L_{\odot}$ and $T_{\text{eff}} = 4000$ K (solid lines) or 3000 K (dashed lines). The diamonds along the curves correspond to dust mass loss rates of 10^{-12} , 10^{-10} , 10^{-9} , 10^{-8} and $10^{-7} M_{\odot} \text{ y}^{-1}$ (from left to right), with a wind velocity of 14 km s^{-1} . Black bodies fall along the central straight line labelled BB. Right panel: same as left for $(K - [12], [25] - [60])$

As discussed in Sect. 2.4, the S stars located in Regions D and E have very specific properties that may help to identify the origin of their large $60 \mu\text{m}$ excess. First, the prototypical SC stars GP Ori and FU Mon located in Region E have a C/O ratio equal to unity to within 1% (Dominy et al. 1986). Similarly, TT Cen is a rare CS star which exhibits ZrO bands at some times and C_2 bands at other times (Stephenson 1973). According to Stephenson (1973), these variations are probably caused by temperature changes in an atmosphere with a C/O ratio very close to unity, or perhaps even to a secular change in the atmospheric C/O ratio. Most of the stars in Regions D and E are actually SC stars or at least S stars with a large C/O spectral index. Finally, several stars in Region E have very extended shells that are resolved at $60 \mu\text{m}$ and, in one case (RZ Sgr), visible in the optical (Whitelock 1994). All these properties point towards these stars being in a very rare and short-lived evolutionary phase. Based on this evidence, we suggest that the large $60 \mu\text{m}$ excess of SC stars

populating Regions D and E finds a natural explanation in the much debated concept of interrupted mass loss first proposed by Willems & de Jong (1988). The cessation of mass loss when C/O gets close to unity (because all C and O atoms are then locked into the CO molecule instead of being involved in dust-forming molecules) causes the dust shell to detach from its parent star, and to cool down as it expands into the interstellar medium without being replenished at its inner side. As shown by Willems & de Jong (1988) and Chan & Kwok (1988), the colors of the dust shell then describe a counter-clockwise loop in the color-color diagram, starting from the region of stars with silicate emission and ending close to the photospheric point (Region A) when the shell has dissolved into the interstellar medium, after passing through Region E. The mass loss resumes when C/O reaches values above unity, and the star then enters the region of heavily-obscured infrared carbon stars (Chan & Kwok 1988; lower VII in Fig. 13). The SC stars found in that region (RZ Peg, UY

Cen and BH Cru, a sister case of TT Cen uncovered by Lloyd Evans 1985) may actually be on the lower part of that loop. The application of the Willems & de Jong scenario (implying that the loop described in the color-color diagram corresponds to a brief evolutionary phase) to the rare, supposedly short-lived SC phase would thus not face the difficulty of inconsistent time scales generally used to argue against it (e.g., Zuckerman & Maddalena 1989). Further support for this idea comes from the peculiar CO line profiles observed for many of the stars populating Region E (FU Mon: see Fig. 15 below; DK Vul, RZ Sgr, TT Cen and UY Cen: Sahai & Liechti 1995), as discussed in Sect. 6.3.

5. Molecular line data and mass loss rates

5.1. New CO data

Observations of the CO(2–1) line at 230 GHz and of the CO(3–2) line at 345 GHz were made in January 1996 and January 1997 with the 10.4 m telescope of the Caltech Submillimeter Observatory (CSO) on Mauna Kea, Hawaii. The CSO is equipped with SIS junction receivers cooled to liquid helium temperatures. The effective single-sideband system temperatures for these observations, including the effects of atmospheric emission and absorption, were about 500 K and 800 K at 230 and 345 GHz, the telescope half-power beamwidths were respectively 30'' and 20'' and the main-beam efficiencies 76% and 65%.

The spectra were observed using two 1024 channel acousto-optic spectrographs (AOS) simultaneously. The first has a total bandwidth of ~ 500 MHz (~ 800 km s $^{-1}$ at 230 GHz) and a velocity resolution of ~ 1 km s $^{-1}$. The second has a bandwidth of ~ 50 MHz and a velocity resolution of 0.1 km s $^{-1}$. The observations were made by chopping between the star position and an adjacent sky position, offset 90'' in azimuth, at a rate of 1 Hz, and consisted of pairs of chopped observations with the source placed alternately in each beam. The spectral baselines resulting from this procedure are linear to within the r.m.s. noise. The telescope pointing errors were measured by mapping the spectral line emission from a nearby CO bright star before each observation was made, and the pointing accuracy is better than $\sim 5''$ for all of the observations.

The temperature scale and atmospheric opacity were measured by chopping against a hot (room temperature) load. The line temperature was corrected for the main-beam efficiency, and the resulting scale is the Rayleigh-Jeans equivalent main beam brightness temperature T_{MB} , i.e. that measured by a perfect 10.4 m antenna above the atmosphere. The spectrometer frequency was calibrated using an internally generated frequency comb, and the velocity scale is corrected to the Local Standard of Rest (LSR).

Twelve S stars were observed at the CSO (Table 4), nine in the CO(2–1) line and three in the CO(3–2) line,

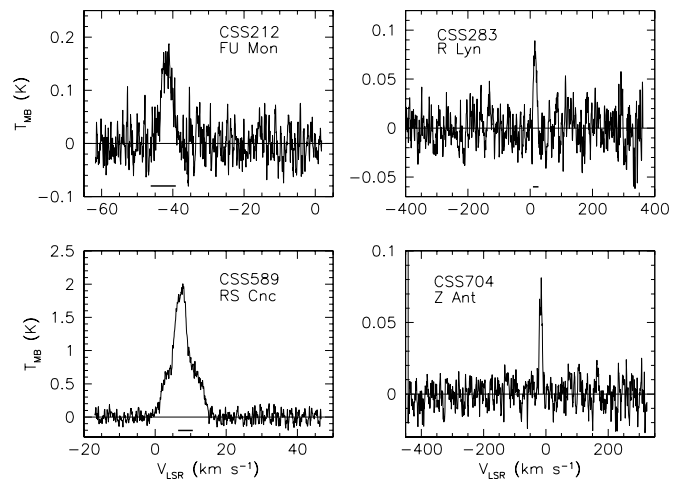


Fig. 14. CO(2-1) line profiles of four S stars observed at CSO. The abscissa is velocity with respect to the LSR and the ordinate main beam brightness temperature. The profiles for GCGSS 212 and 589 are observed with a velocity resolution of ~ 0.1 km s $^{-1}$, while GCGSS 283 and GCGSS 704 are observed with 1 km s $^{-1}$ resolution. The horizontal bars show the velocity range observed in optical spectra (Table 4). There is no optical velocity available for GCGSS 704

and emission was detected from four (Table 5). The line profiles for the detected stars are shown in Fig. 14.

Table 4 lists the stars that were observed: the GCGSS number and the variable star name are in columns 1 and 2, respectively. Next is the observed position: we used positions accurate to $\sim 1''$ from the HST Guide Star Catalog and other sources (see Chen et al. 1995). Columns 5–9 list the galactic longitude and latitude, the spectral type from the GCGSS, the variable type and the period from the GCVS. Column 10 gives the stellar radial velocity with respect to the LSR measured from optical spectra; since the radial velocities of red giants vary as they pulsate, Table 4 lists the range of reported radial velocities. Finally, column 11 gives the channel-to-channel r.m.s. noise in the 500 MHz AOS.

Table 5 gives the line parameters of the four detected stars: the CO(2–1) line flux in K \times km s $^{-1}$, the peak line temperature, the central velocity V_c and the half-width of the line at zero power, V_e , which gives the terminal wind outflow speed. These quantities are determined by fitting a parabolic line model to the data. The agreement between the optical and CO radial velocities is good.

Seven of the stars in Table 4, GCGSS 89, 117 (GP Ori), 422 (NQ Pup) 626 (FM Hya), 704 (Z Ant), 796 (HR 4755) and 803 (S UMa) have not previously been observed. We detect one of these, Z Ant. GCGSS 816 (UY Cen) is weakly detected by Sahai & Liechti (1995, SL95) with good agreement between the CO and optical radial velocities. This

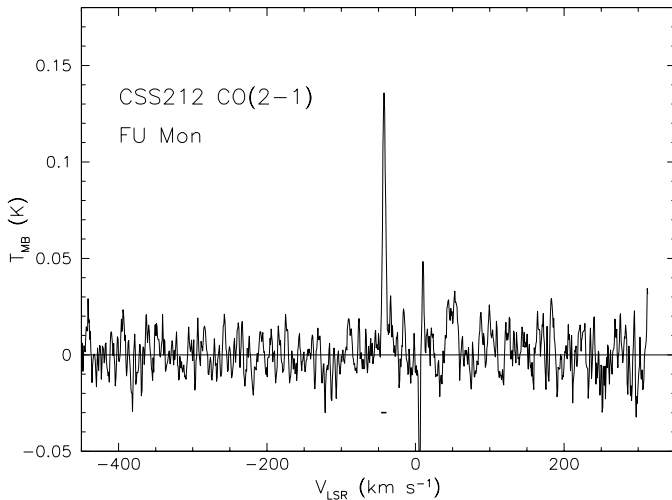


Fig. 15. Broad-band CO(2-1) spectrum in the direction of GCGSS 212 (FU Mon). The horizontal bar shows the range of the observed optical velocities

star was not detected in the present observations, but our sensitivity is lower. The detection of circumstellar CO for this star is of particular interest, given its rare SC spectral type (see Sect. 6.3). GCGSS 149 (NO Aur) and 796 (HR 4755) were previously observed by SL95 and by Bieging & Latter (1994, BL94); like the present observations, these did not detect CO emission.

RS Cnc has been observed by many authors (see Loup et al. 1993, for example). Margulis et al. (1990) point out that the CO line profile for this star, as for several others, more closely resembles a triangle or gaussian in shape than the parabolic profile typical of circumstellar winds. The high velocity resolution observations in Fig. 14 show that the line profile actually consists of two parabolic components of different widths centered at the same velocity. The parameters for these profiles, estimated by eye, are given in Table 5. This line shape may indicate the presence of two molecular winds. Such line profiles have been seen for several other stars (e.g. Margulis et al. 1990, SL95, Kahane & Jura 1996, Knapp et al. 1997a) and may be quite common.

GCGSS 283, R Lyn, has previously been detected by BL94, and the data in Table 5 are in good agreement. FU Mon (GCGSS 212) was detected by SL95, who observe two narrow features at -44 and $+14$ km s^{-1} which they attribute to the blue- and red-shifted components of an expanding circumstellar shell. However, the optical radial velocity of the star is about -43 km s^{-1} (Table 4), and further, the narrow component at $+14$ km s^{-1} is likely to be interstellar, as shown by our observations with the 500 MHz AOS in Fig. 15. We conclude that the emission at -44 km s^{-1} (best seen on the high resolution profile in Fig. 14) is from the circumstellar envelope. The out-

flow speed, 3 km s^{-1} , is very low, but similar low values are found for some other Mira and semi-regular variables (Young 1995; Kerschbaum et al. 1996).

5.2. CO data from the literature

Table 6 summarizes (under the header ‘Observations’) CO millimeter wavelength observations of S stars published since 1990, including those in the present paper. Data observed prior to 1990 can be found in Loup et al. (1993). The stars in Table 6 are grouped according to their location in the $(K - [12], [25] - [60])$ color-color diagram (see Sect. 2.3) and arranged in order of right ascension within these groups. Several observations are not listed in Table 6 because they were made at positions which are too discrepant from the optical position; the stars are GCGSS 133, GZ Peg, and T Cam.

Table 6 gives the IRAS name (an asterisk before the IRAS name refers to a note at the end of the table), the star name and the results of CO observations of the star: the line observed; the telescope half power beamwidth in arcseconds; the channel-to-channel r.m.s. noise in K; the integrated line brightness in $\text{K} \times \text{km s}^{-1}$; the peak brightness temperature in K; the central velocity V_c with respect to the LSR; the wind outflow speed V_e ; and the reference. All temperatures are expressed in main-beam brightness temperature. Dashes for any of these quantities mean either that no emission was detected from the star or that the quantity in question was not quoted in the paper. Table 6 contains observations of 56 stars, with 35 detections.

To first order, the peak brightness temperatures and the integrated CO line intensities should scale inversely with the square of the telescope beamwidth, since the CO lines are usually fairly optically thick and the envelopes in general smaller than the beam. As Table 6 shows, this is roughly the case, and the agreement among the observations is in general good, with no serious discrepancies.

Figure 16 shows the histogram of the stellar systemic radial velocities (with respect to the LSR). The values adopted for stars with multiple observations are straight averages of the individual values. The mean velocity for S stars detected in CO is $\langle V \rangle = -9.1 \pm 5.0$ km s^{-1} and the radial-velocity dispersion is $\sigma = 25.9 \pm 4.5$ km s^{-1} . This value refers to a sample of intrinsic S stars, since no extrinsic S stars have been detected in CO. This dispersion is typical of a young-disk population (Mihalas & Binney 1981). Such a population should have a scale-height above the galactic plane of about 200 pc, in agreement with the results of Van Eck et al. (1997).

Figure 17 shows the histogram of the wind terminal velocity V_e compared with the distributions for three other sets of molecular line observations; those for nearby oxygen-rich Mira variables (Young 1995), for semi-regular (SRa and SRb) variables (Kerschbaum et al. 1996) and for carbon stars (Olofsson et al. 1993). The outflow speeds V_e for the S stars are taken from Table 6. We used average

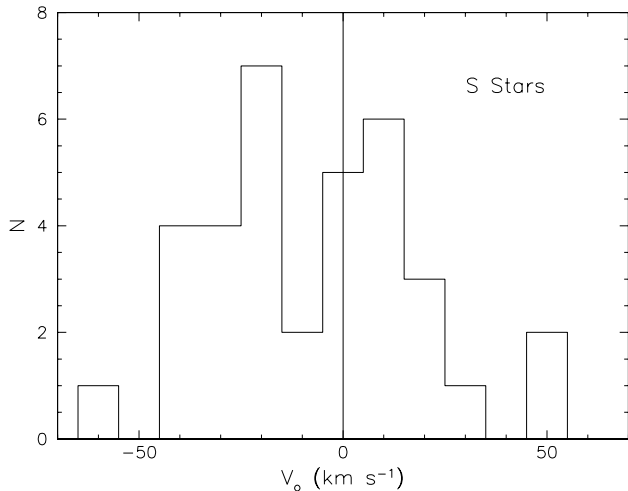


Fig. 16. Distribution of radial velocities (with respect to the LSR) from CO observations of intrinsic S stars

values for stars with multiple observations except for RZ Sgr (20120–4433), for which CO(1–0) and (2–1) observations give discrepant values (14 and 8.8 km s^{−1}; SL95). We use the velocity derived from the CO(2–1) observation since this has a much higher signal-to-noise ratio, but note that the CO(1–0) line may really be broader; the larger telescope beam at this wavelength could be detecting gas at larger distances from the extended envelope of this star, which could have a larger outflow velocity.

Figure 17 shows that oxygen-rich Miras have the smallest outflow velocities (median 6.5 km s^{−1}, largest value 12.7 km s^{−1}), while those of the SRVs cover a similar range (median 8.0 km s^{−1}, largest value 15.6 km s^{−1}). Carbon stars have the largest outflow velocities (median 12.0 km s^{−1}, largest value 33.2 km s^{−1}) while as expected S stars are intermediate (median 8.5 km s^{−1}, largest value 24.7 km s^{−1}). The largest V_e in our sample of S stars is observed for the CS star TT Cen, a border case between S and C stars (see Sect. 2.1). Figure 18 shows that, among Mira S stars, the outflow velocity correlates well with the period of the photometric variations, a result already discussed by Heske (1990) and by Olofsson et al. (1993). Jura (1988) finds an almost identical dependence on period for the ratio of flux densities at 25 and 2.2 μm .

5.3. Mass loss rates

The CO data from Table 6 were used to calculate mass loss rates for the detected S stars and upper limits for the non-detected stars. The CO lines were modeled using a code based on that of Morris (1980) which assumes spherically-symmetric mass loss at a constant rate and

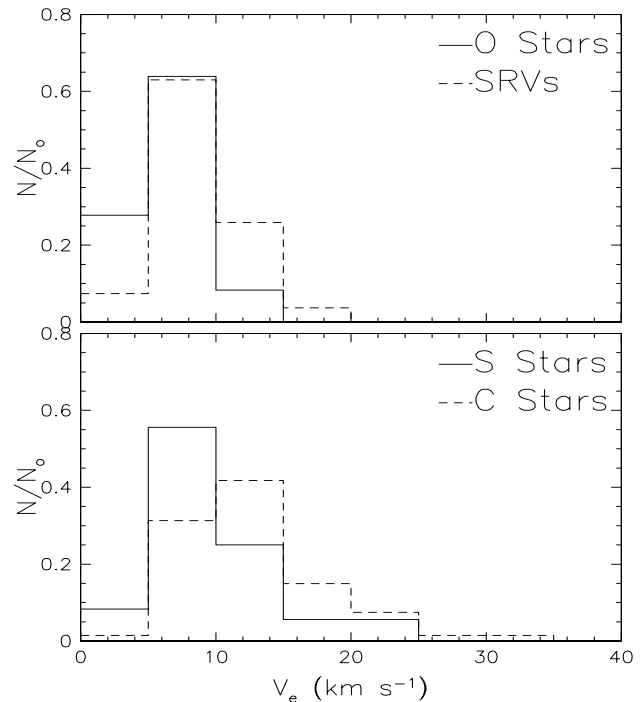


Fig. 17. Normalized histogram of terminal wind outflow speeds of (a) oxygen-rich Miras (Young 1995) and semiregular variables (Kerschbaum et al. 1996) and (b) S stars (present work) and carbon stars (Olofsson et al. 1993)

constant outflow speed² with excitation by collisions and by infrared photons at 4.6 μm . The envelope outer radius was taken to be that at which the CO is photodestroyed by the diffuse interstellar radiation field using the calculations of Mamon et al. (1988). The details are given by Knapp et al. (1997b). The relative abundance of CO to H₂ was assumed to be 6.5×10^{-4} for all stars (Lambert et al. 1986; Smith & Lambert 1990).

The infrared radiation field was approximated as that of a black body of temperature 2500 K and radius 2.5 10^{13} cm. Models show that the CO line strength is only weakly dependent on the radiation field, so this simplifying assumption is unlikely to produce an uncertainty of more than 20% in the derived mass loss rates.

The distances are derived by adopting absolute magnitudes which depend on location in the IR color-color diagram. For stars in Region A (photospheric colors) we assume $M_{\text{bol}} = -2$, i.e. one magnitude below the RGB tip for solar-metallicity stars with $M = 1 M_{\odot}$ (Schaller et al. 1992). The bolometric correction $M_{\text{bol}} - M_K$ is derived from the apparent bolometric flux for BD Cam (HR 1105) obtained by integrating the flux densities corresponding to the *UBVRIJKL* magnitudes from Lee (1970) plus the IRAS flux densities. The corresponding absolute *K* mag-

² The mass loss rates estimated in the present paper might therefore be inadequate for those stars in Regions D and E with a resolved – possibly detached – shell as observed at 60 μm

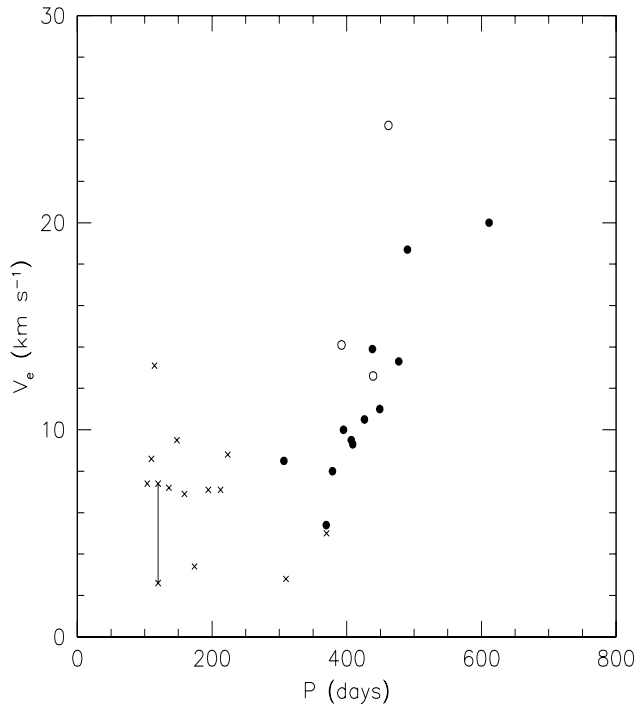


Fig. 18. Terminal wind outflow speed of S stars measured from CO millimeter wavelength emission lines versus period of photometric variations (from the GCVS). Circles: Mira variables (open circles are for stars for which there is only one measurement of V_e); crosses: semi-regular variables. The points corresponding to the two outflow speeds for RS Cnc are connected by a vertical line. The data for DY Gem, 06331+1414 (SRa; $P = 1145$ d), are not included in the figure

nitude is -4.6 . Other authors, e.g. Jura (1988) have used $M_K = -8.1$ for all S stars; this absolute magnitude is derived from carbon stars in the solar neighborhood and AGB stars in the Magellanic Clouds.

For stars in the other regions, which are supposedly more evolved than are those in Region A, we adopt $M_K = -8.1$. That value of M_K yields distance moduli that are consistent with direct determinations when available. For the composite system π^1 Gru (S5,7e + G0V), Ake & Johnson (1992) derive a distance modulus of 6.0 from a fit to the UV spectrum, corresponding to a distance of 160 pc, identical to the value derived from the K magnitude (Table 1). For T Sgr, a distance of 1000 pc (as compared to 810 pc from the K distance modulus) is derived by Culver & Ianna (1975) from the spectral type F3IV assigned to its companion. For χ Cyg, a distance of 136 pc is obtained from the distance modulus in the K band, consistent with that (106 pc) derived from the Hipparcos parallax ($\pi = 9.43 \pm 1.36$ mas; van Leeuwen et al. 1997).

The evolutionary status of stars in Regions D and E is unclear, as is their relationship to stars in other regions of the color-color diagram, and so their absolute magnitudes are uncertain. Since these are generally stars of spectral

type SC, the choice $M_K = -8.1$ appears to be a reasonable one.

We modeled the wind from RS Cnc as two separate components, fit only to the CO(2–1) observations described in the previous section.

The upper limits to the mass loss rate of S stars not detected in CO were calculated using the median outflow speed of 8.5 km s^{-1} found for the detected sample and assuming that we can detect a line of brightness temperature three times the r.m.s. noise (examination of the data in Table 6 suggests that this is reasonable).

The best fit mass loss rates were found by calculating the model peak antenna temperature and integrated line intensities for a given input mass loss rate and comparing it with the observations. The mass loss rates were adjusted until reasonable agreement with all of the observations was found, and were corrected for the mass of helium (see Knapp & Morris 1985).

The results are listed in the rightmost columns of Table 6 (under the header ‘Model’), which list the distance, the mean outflow speed (the same for all lines; the value of 8.5 km s^{-1} used for calculating the upper limits is given in parentheses), the CO photodissociation radius in cm and in arcseconds, and the predicted CO peak line temperature and integrated CO line intensity for each of the observed lines. Comparison between the calculations and observations shows that uncertainties in the observations introduce about a factor of two uncertainty into the mass loss rate.

6. Discussion

6.1. Comparison with mass-loss rates of Oxygen and Carbon stars

Several authors (e.g. Netzer & Elitzur 1993; Young 1995) have shown that AGB stars with higher mass loss rates have higher outflow velocities. The corresponding relationship for S stars is shown in Fig. 19 and compared with the results for oxygen-rich Miras (Young 1995) and carbon stars (Olofsson et al. 1993). The relationship between V_e and \dot{M} found for oxygen stars by Young (1995) is also shown.

It is not clear at present whether the relationship between V_e and \dot{M} demonstrated by these data is real, in the sense that it has a physical origin, or is due to selection effects. For the present purpose, we will simply treat it as a convenient way to display the data and compare samples. The mass loss rates in Fig. 19 have been calculated assuming a CO abundance of $f = n(\text{CO})/n(\text{H}_2) = 3 \times 10^{-4}$ for oxygen stars (Young 1995), 6.5×10^{-4} for S stars and 9×10^{-4} for carbon stars (Olofsson et al. 1993). The S and oxygen stars show essentially the same correspondence between \dot{M} and V_e (though there is a lot more scatter in the S star data), giving some confidence in the assumed value of f and the resulting mass loss rates. The apparently

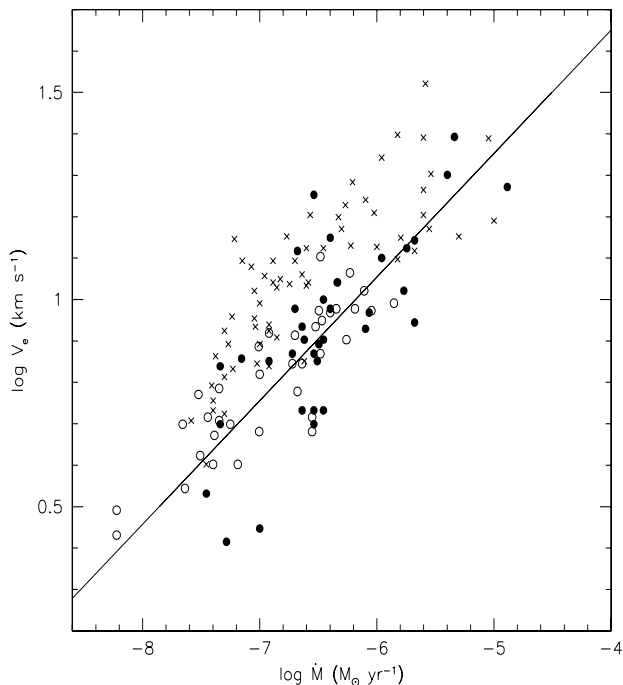


Fig. 19. Wind outflow speed V_e versus mass loss rate for: open circles: oxygen-rich Miras (Young 1995); filled circles: S stars (current work); crosses: carbon stars (Olofsson et al. 1993). The relationship for oxygen Miras found by Young (1995) is also shown

higher values of V_e for a given mass loss rate for carbon stars (see also Fig. 17) will be discussed elsewhere.

6.2. Comparison of mass loss rates and color excesses

The color excess can also be used to give the mass loss rate if the gas-to-dust ratio and the outflow speed are known. This is illustrated in Fig. 20, which shows the envelope density \dot{M}/V_e versus the $12\mu\text{m}/2.2\mu\text{m}$ color. At low mass loss rates ($\dot{M} \leq 10^{-7} M_\odot \text{y}^{-1}$) the broad-band colors are dominated by the colors of the photosphere, as expected, while the stars with higher mass loss rates show a strong correspondence between the mass loss rate and the $12\mu\text{m}$ color, showing that the gas to dust ratio in these envelopes is roughly constant. The relationship in Fig. 20 is in agreement with that for oxygen stars shown by Habing (1996).

The two stars TT Cen and RZ Sgr in Region E markedly depart from this relationship, however. These are probably in a transitory phase of evolution; TT Cen is a rare CS star where ZrO bands seem to have disappeared while C_2 bands appeared (see Sect. 2.1 and Stephenson 1973), while RZ Sgr is surrounded by an optical (White-lock 1994) and IR (YPK) nebula.

Stars with roughly photospheric $12\mu\text{m}/2.2\mu\text{m}$ colors show a wide range in envelope densities. This large scatter may be due to the imperfect coupling between dust and gas at these low densities, which sets a lower limit to the

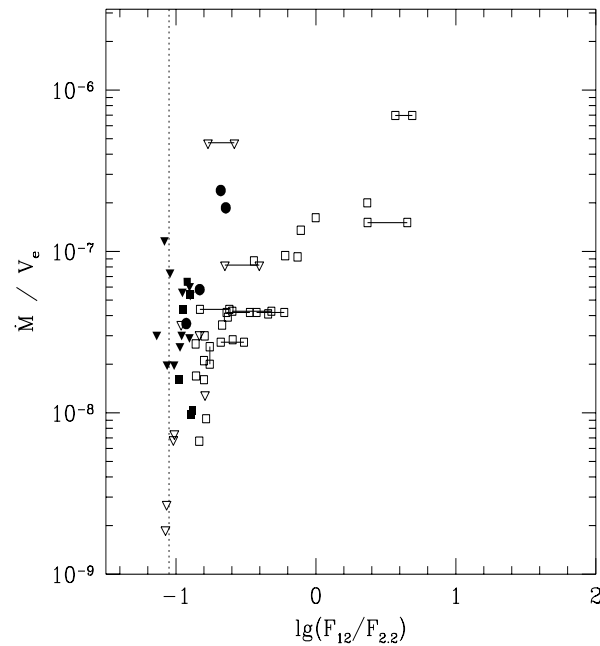


Fig. 20. Envelope density \dot{M}/V_e (measured in $M_\odot \text{y}^{-1}$ and km s^{-1}) versus the ratio of $12\mu\text{m}$ to $2.2\mu\text{m}$ flux densities. The vertical dotted line shows the photospheric color for a star of temperature 3000 K. Open symbols: stars in Regions A, B and C of the IR color-color diagram (Fig. 3); filled squares: stars in Region D; filled circles: stars in Region E. The inverted triangles show upper limits

mass loss rate for a radiation-pressure driven wind (cf. Netzer & Elitzur 1993; SL95). Empirically, this limit is a few $10^{-8} M_\odot \text{y}^{-1}$ (Fig. 20 and Table 6).

6.3. Mass loss rates and the IRAS color-color diagram

Figure 21 presents the mass loss rates of S stars as a function of their location in the $(K - [12], [25] - [60])$ diagram. None of the stars in Region A (stars with photospheric colors) has detectable circumstellar CO emission, with limits on the mass loss rates of $< 6 \times 10^{-8} M_\odot \text{y}^{-1}$ and envelope densities well below those of the detected stars (Fig. 20). This confirms the lower limit at which a star can lose mass by a radiation-pressure driven wind estimated by Netzer & Elitzur (1993). The low mass-loss rates inferred for extrinsic S stars in Region A also confirm an earlier suggestion (Paper I) that these stars are less evolved than the intrinsic S stars populating the other Regions of the IR color-color diagram.

Stars in Regions B and D have moderate mass loss rates, in the range 5×10^{-8} to $5 \times 10^{-7} M_\odot \text{y}^{-1}$. One star from Region B (RS Cnc) has been found to exhibit a double wind (Table 6). Most of the observed stars, and most of the detections, lie in Region C, which contains stars with moderately optically thick circumstellar envelopes, likely containing silicate dust. CO emission is detected from 20

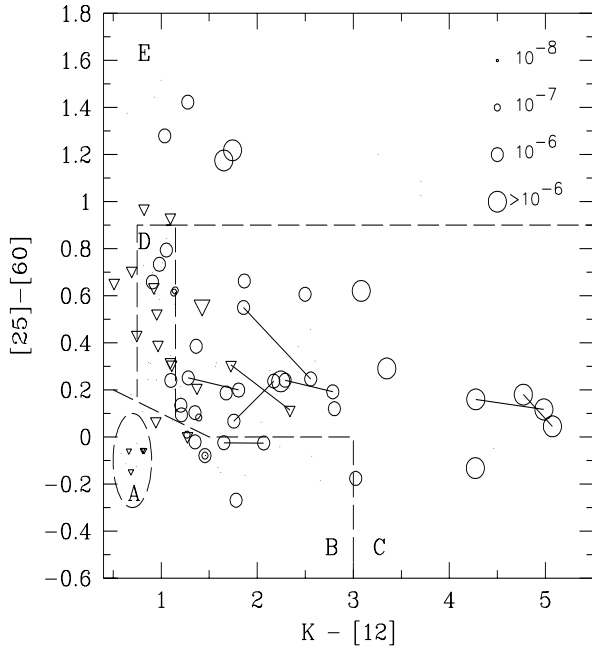


Fig. 21. Mass loss rates of S stars (as measured from CO) in the $(K - [12], [25] - [60])$ diagram. The diameter of the circle is proportional to the mass loss rate, as labeled. Inverted triangles correspond to upper limits

of these 23 stars, and the mass loss rates are typically larger than several $\times 10^{-7} M_{\odot} \text{ y}^{-1}$. The undetected stars have upper limits greater than this value, so that the data are consistent with the conclusion that all stars in this region lose mass at a rate larger than several $10^{-7} M_{\odot} \text{ y}^{-1}$.

The stars in Region D, which show roughly photospheric $12\mu\text{m}/2.2\mu\text{m}$ colors despite large $[25] - [60]$ indices, generally have low mass-loss rates (like Region B). Stars in Region E have mixed properties. Some, like TT Cen and RZ Sgr, lose mass at a very large rate (several $10^{-6} M_{\odot} \text{ y}^{-1}$), while others like FU Mon lose mass at a more moderate rate (a few $10^{-7} M_{\odot} \text{ y}^{-1}$). Figure 22 presents the variation of the wind velocity across the $(K - [12], [25] - [60])$ diagram, and shows that stars in Region E also have a wide range of wind velocities, from very low (FU Mon: 2.8 km s^{-1}) to very large (TT Cen: 24.7 km s^{-1}).

FU Mon also has a resolved IR envelope (Sect. 2.4), and this fact taken together with a low mass loss rate and a small outflow velocity suggest that mass loss has just resumed in that star. Olofsson et al. (1990; 1993) detected several carbon stars (S Sct, U Ant, TT Cyg) with a detached shell and a double wind that would also fall in our Region E. The older, detached shell was produced by a massive, fast wind, whereas the recent shell is caused by a slow (5 km s^{-1}), low mass loss rate wind. Since FU Mon is an SC star with a C/O ratio close to unity (Dominy et al. 1986), the mass loss may have come to a halt when the

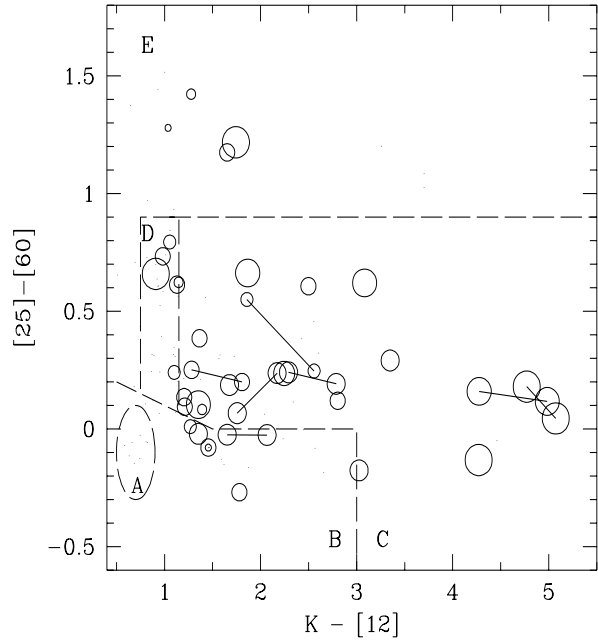


Fig. 22. The outflow velocity as measured from CO for S stars in the $(K - [12], [25] - [60])$ diagram. The diameter of the circle is proportional to the outflow velocity. Compare to Fig. 10 of Olofsson et al. (1993) for C stars

the C/O ratio approached unity, as already suggested by Willems & de Jong (1988) and Chan & Kwok (1988). This scenario may well hold for all SC stars, even though some, like UY Cen, are in fact located in Region C. As argued in Sect. 4.2, that star may be at the end of the loop in the IR color-color diagram. The horn-shaped CO line profile of UY Cen observed by SL95, indicative of a detached shell and fossil mass loss, supports this idea. Finally, other stars lying in Region E like TT Cen, RZ Sgr and DK Vul have peculiar CO line profiles (narrow central feature superimposed on a broader less intense feature) suggesting that they have multiple winds.

6.4. Mass loss rates and binaries

Several intrinsic S stars in the sample considered in this paper are binaries with main sequence companions, as revealed by the composite nature of their spectrum at minimum light (WY Cas, W Aql, T Sgr; Herbig 1965; Culver & Ianna 1975). A composite spectrum is also suspected for S Lyr from its shallow lightcurve (Merrill 1956). The star π^1 Gru has a close G0V visual companion (Feast 1953). W Aql, WY Cas and S Lyr are surely among the S stars with the largest mass loss rates, while T Sgr and π^1 Gru have mass loss rates close to the average for stars in Region C. Clearly, a definite conclusion as to whether binarity can indeed reinforce the mass loss rate, e.g. by the companion-

reinforced attrition process (Eggleton 1986), would require the knowledge of the orbital separation of these systems.

It has sometimes been argued (e.g. Eggleton 1986; Tout & Eggleton 1988; Kenyon 1994; Han et al. 1995) that the mass loss rates of giant stars in binary systems must be larger than those of single red giants. More precisely, Han et al. (1995) suggest that the mass loss rate of a giant approaching its Roche lobe in a binary system exceeds by more than a factor 10^3 the rate predicted by the Reimers formula (Reimers 1975). As far as the binary, extrinsic S stars are concerned, this effect, if present, is clearly not large enough to bring their mass loss rates to the level of the intrinsic S stars. The difference in the evolutionary stages of extrinsic and intrinsic S stars, believed to be RGB (or Early-AGB, according to the terminology of Iben & Renzini 1983) and TP-AGB stars, respectively, thus appears to be of greater importance for the mass loss rate than their binary or non-binary character.

7. Summary

Our extensive discussion of the circumstellar properties of S stars confirms the dichotomy extrinsic/intrinsic S stars and leads to the following conclusions.

Extrinsic S stars have the lowest mass loss rates among S stars ($< 2 \cdot 10^{-8} M_{\odot} \text{ y}^{-1}$), and undetectable circumstellar shells. This is consistent with the hypothesis that these stars are much less evolved than intrinsic S stars, populating the RGB or Early-AGB rather than the TP-AGB like intrinsic S stars. The binary character of these stars does not seem to increase their mass loss rate, as it has sometimes been suggested, e.g., in discussions relating to symbiotic or barium stars. Note, however, that the few binary intrinsic S stars are among the stars with the largest mass loss rates in our sample.

Among *intrinsic* S stars, various subclasses must be distinguished:

1. A few Te-rich S stars (e.g., HR Peg) have very low mass-loss rates, similar to those of the extrinsic S stars, with undetectable circumstellar shells [Region A of the ($K - [12]$, $[25] - [60]$) color-color diagram]. These are S stars with weak chemical peculiarities, barely distinguishable from normal M giants.
2. S stars with weak chemical peculiarities and tenuous O-rich circumstellar shells (small $K - [12]$ excess), fed by a small albeit measurable mass loss rate of a few $10^{-7} M_{\odot} \text{ y}^{-1}$ (Region B). These are short-period ($P \sim 100$ to 150 d) SR variables or short-period ($P < 500$ d) Mira variables. This region may be contaminated by (possibly normal M) supergiants of variability type SRc (T Cet, RS Cnc, Y Lyn). These SRc supergiants have resolved shells at $60 \mu\text{m}$, and for RS Cnc, a double wind.
3. S stars with strong chemical peculiarities and dense O-rich circumstellar shells (as indicated by SiO maser emission, the $9.7 \mu\text{m}$ silicate feature and large $K - [12]$ indices), populating the lower part of Region C. Mass loss

rates range from several 10^{-7} to $10^{-5} M_{\odot} \text{ y}^{-1}$. Almost all of them are long-period ($P > 300$ d) Mira variables.

4. S stars with strong chemical peculiarities (often classified as SC in the optical), with neither SiO maser emission nor $9.7 \mu\text{m}$ silicate emission, with featureless IRAS spectra and moderate to large $[25] - [60]$ indices. These stars populate Region D and the upper part of Region C (like optical carbon stars) and have moderate mass loss rates (a few 10^{-8} to a few $10^{-7} M_{\odot} \text{ y}^{-1}$) with small wind velocities (generally $\lesssim 8 \text{ km s}^{-1}$). They are mainly semi-regular (with periods ranging from 60 to 360 d) or irregular variables, with a few short-period ($P < 370$ d) Mira variables. These properties are reminiscent of carbon stars. All their features may equally well be explained by a carbon-rich circumstellar shell, or by a detached shell. The relationship between stars in Regions C and D is far from being clear. It may be a difference of galactic populations, as suggested by their different properties as variable stars, or stars might oscillate between Regions C and D at different phases of their variability cycle, as observed for some variable IRAS sources in our sample, or they may be on different parts of the loop associated with the detachment of a dust shell.

5. A few S stars have well-resolved (and thus very extended) IR shells (also visible in the optical in the case of RZ Sgr), probably detached from their parent star, as indicated by strong 60 and $100 \mu\text{m}$ excesses (Region E). The mass loss rates span a wide range, from a few 10^{-7} to several $10^{-6} M_{\odot} \text{ y}^{-1}$, as do the wind velocities (25 km s^{-1} for TT Cen to 2.8 km s^{-1} for FU Mon). These stars with extreme properties are often SC or CS stars, and may be experiencing a loop in the IRAS color-color diagram as first proposed by Willems & de Jong (1988), triggered by their C/O ratio being very close to unity. In TT Cen, the dominant spectral features are ZrO bands at some times, and C_2 bands at other times. This is a rare and short-lived phase, and thus does not face the difficulties generally opposed to the Willems & de Jong scenario. Some SC or CS stars in Region C, like BH Cru (a sister case of TT Cen) and UY Cen, may be at the end of the counter-clockwise loop in the IRAS color-color diagram, entering the region of heavily-obscured IR carbon stars. Region E is probably fed by stars leaving Region C when their C/O ratio reaches values close to unity. However, there is no need that all S stars experience such a loop.

Acknowledgments. We thank the staff at CSO, especially Ken Young (Taco), Antony Schinkel, Maren Purves and Tom Phillips, for the observing time and for their help with the observations. Astronomical research at the CSO is supported by the National Science Foundation via grants AST96-15025. We thank the staff at IPAC for swiftly processing the numerous requests for IRAS archive data sent over the Internet. We especially thank Ron Beck for providing us with the IRAS template data. We thank Princeton University, the *Fonds National de la Recherche Scientifique* (Belgium) and the National

Table A1. IRAS flux densities for χ Cyg

$JD - 2440000$	ϕ	F_{12} (Jy)	offset ($'$)	det	F_{25} (Jy)	F_{60} (Jy)	[12]–[25]	[25]–[60]
5452.8	0.12	1860.6	0.40	48	643.5	99.4	0.41	–0.15
					540.2		0.22	0.04
5453.7	0.12	1778.6	–1.01	23	533.2	97.7	0.25	0.04
		1880.7	1.23	51		92.6	0.19	–0.02
5466.1	0.15	1157.5	–1.79	28	626.6	86.5	0.89	–0.27
		1975.0	0.63	48	525.0	99.8	0.37	–0.11
							0.70	–0.08
							0.18	0.08
5466.2	0.15	1624.5	–0.03	53	520.7	98.7	0.32	0.08
					583.0		0.45	–0.05
5639.7	0.58	1248.7	–0.22	30	456.3	72.6	0.47	–0.11
					422.1		0.38	–0.03
5639.8	0.58	1172.5	–0.52	24	433.5	69.5	0.48	–0.11
		1266.5	1.72	49			0.40	
5640.3	0.58	1184.6	–0.04	24	404.9	70.8	0.39	–0.01
5640.6	0.58	1249.0	0.13	27	383.0	74.7	0.28	0.11
		1214.4	1.75	51			0.31	

Science Foundation (USA), via grant AST96-18503, for partial support of this work. The CO line formation modeling was based on code by Mark Morris, and the figures were drawn using software by Robert Lupton and Patricia Monger. This research has made use of the Simbad data base, operated at CDS, Strasbourg, France. A.J. is Research Associate, F.N.R.S. (Belgium).

Appendix A: Stellar variability and the IRAS flux densities

As discussed in Sect. 2.2, the flux densities obtained from co-addition of the IRAS data generally agree well with those in the PSC with, however, some notable exceptions, as shown in Fig. 1. Several stars have flux densities which are in disagreement at a level well outside that expected from noise. In this Appendix we investigate whether these disagreements can be explained by stellar variability, using the data for χ Cyg as an example. The ephemerides listed in the GCVS give a variation of about 6 mag at V between maximum and minimum light, a period of 408 d and the epoch of zero phase which is closest to the IRAS launch date of JD 2445404.4.

The colors of χ Cyg, calculated from the IRAS PSC flux densities (see Table A2), are photospheric, despite the strong circumstellar CO emission (discussed in Sect. 5). On the other hand, model IRAS colors calculated from the mass loss rate given by the CO lines (several $10^{-7} M_{\odot} \text{ y}^{-1}$), assuming a normal gas to dust ratio and silicate grains (the star is an SiO maser; e.g. Patel et al. 1992), are well displaced from photospheric values. This discrepancy does *not* mean that the circumstellar envelope is dust-free, however; the ratio of the $12\mu\text{m}$ to $2\mu\text{m}$ flux

densities is well in excess of the photospheric value for a temperature of 2400 K (Haniff et al. 1995), demonstrating the presence of an appropriate amount of circumstellar dust.

We therefore re-examined the raw IRAS data for this star. The individual IRAS $12\mu\text{m}$, $25\mu\text{m}$, and $60\mu\text{m}$ observations for χ Cyg are listed in Table A1. Column 1 gives the Julian date of the observations computed from the ‘Satellite Operation Plan’ number attached to each scan and from the mission chronology provided by the *Explanatory Supplement*. Column 2 lists the phase. Next are the flux density, the offset between the scan center and the stellar position, and the detector number for the $12\mu\text{m}$ data. The final columns contain the $25\mu\text{m}$ and $60\mu\text{m}$ flux densities and the [12] – [25] and [25] – [60] colors calculated from combinations of the observed flux densities. The colors calculated from the flux densities derived from individual scans locate χ Cyg in Region B of the color-color diagram.

Table A1 shows that there are occasionally large discrepancies between the flux densities measured by different detectors at the same time; see, for example, the $12\mu\text{m}$ flux densities observed at JD2445466.1. The low flux density is probably due to the large offset between the stellar and detector center positions; such discrepant observations are usually filtered out in the IRAS data processing. Real variability is also apparent. The data were obtained at two epochs, near maximum and minimum phase, and the flux densities at all four wavelengths are systematically higher for the first set of observations than the second. The mean flux densities for these two epochs are listed in Table A2; the differences are $\Delta = (F_{\text{max}} - F_{\text{min}})/F_{\text{max}} =$

32% at 12 μm , 26% at 25 μm , 25% at 60 μm and 31% at 100 μm .

Can these variations be attributed to the stellar variability? The huge variations in Mira variables at visible wavelengths are due largely to the changing photospheric temperature; the variation in the bolometric magnitude is much smaller, about a factor of 2 (e.g. Petit 1982; Hoffmeister et al. 1985). Because of the variation in stellar effective temperature, the star reaches maximum light later at longer wavelengths in the visible and near infrared (e.g. Le Bertre 1992). In particular, the variation at visible wavelengths leads the total light variation by about 0.1 of a period. The two groups of observations in Table A1 were thus made close to maximum and minimum luminosity.

We modeled the object as a star with a circumstellar envelope and varied the luminosity of the model star. The envelope contains silicate grains, has a dust loss rate of $8 \cdot 10^{-10} M_{\odot} \text{ y}^{-1}$ and is assumed to have the same outflow speed as the gas (9.5 km s^{-1}). The star is assumed to be a black body of temperature 2400 K and luminosity $3000 L_{\odot}$ at minimum, and 2800 K and $6000 L_{\odot}$ at maximum. The resulting model flux densities are listed in Table A2 and are reasonably close to the observed values (note that the discrepancy at 12 μm may be caused in part by the saturation of the detectors at these flux densities exceeding 1000 Jy). The variation in the IRAS flux densities can thus be fully explained by the stellar variability.

These results show that caution is required in the interpretation of IRAS data for variable stars; colors must be calculated from data taken at the same epoch, as should models of the circumstellar envelope. Variability introduces a significant amount of scatter into the IRAS colors, especially [12] – [25], which as a result does not provide the clean measure of the stellar mass loss rate which the models predict (see, for example, the discussion by Habing 1996).

Table A2. Observed and model IRAS flux densities for χ Cyg. The PSC fluxes are also listed

Phase	Observed (averages)			
	F_{12} (Jy)	F_{25} (Jy)	F_{60} (Jy)	F_{100} (Jy)
max	1804	568	96	20
min	1223	420	72	14
PSC	1688	459	81	18

Phase	Calculated			
	F_{12} (Jy)	F_{25} (Jy)	F_{60} (Jy)	F_{100} (Jy)
max	1486	576	86	20
min	1108	486	79	17

References

- Ake T.B., Johnson H.R., 1992, BAAS 24, 788
 Beckwith S., Evans N.J., Becklin E.E., Neugebauer G., 1976, ApJ 208, 390
 Benson P.J., Little-Marenin I.R., Woods T.C., Attridge J.M., Blais K.A., Rudolph D.B., Rubiera M.E., Keefe H.L., 1990, ApJS 74, 911
 Bessell M.S., Wood P.R., Lloyd Evans T., 1983, MNRAS 202, 59
 Bieging J.H., Latter W.B., 1994, ApJ 422, 765 (BL94)
 Brown J.A., Smith V.V., Lambert D.L., Dutchover E., Hinkle K.H., Johnson H.R., 1990, AJ 99, 1930
 Catchpole R.M., Robertson B.S.C., Lloyd Evans T.H.H., Feast M.W., Glass I.S., Carter B.S., 1979, SAAO Circ. 1, 61
 Chan S.J., Kwok S., 1988, ApJ 334, 362
 Chen P.S., Gao H., Chen Y.K., Dong H.W., 1988, A&AS 72, 239
 Chen P.S., Kwok S., 1993, ApJ 416, 769
 Chen P.S., Gao H., Jorissen A., 1995, A&AS 113, 51
 Culver R.B., Ianna P.A., 1975, ApJ 195, L37
 Deguchi S., Nakada Y., Forster J.R., 1989, MNRAS 239, 825
 de Jong T., 1989, A&A 223, L23
 Dominy J.F., Wallerstein G., Suntzeff N.B., 1986, ApJ 300, 325
 Draine B.T., 1985, ApJS 57, 587
 Draine B.T., Lee H.M., 1984, ApJ 285, 89
 Epchtein N., Le Bertre T., Lépine J.R.D., Marques Dos Santos P., Matsuura O.T., Picazzio E., 1987, A&AS 71, 39
 Epchtein N., Le Bertre T., Lépine J.R.D., 1990, A&A 227, 82
 Eggleton P.P., 1986. In: Trümper J., Lewin W.H.G., Brinkmann W. (eds.) The Evolution of Galactic X-ray Binaries. Reidel, Dordrecht, p.87
 Feast M.W., 1953, MNRAS 113, 510
 Frost C.A., Lattanzio J.C., 1995. In: A. Noels, D. Fraipont, M. Gabriel, N. Grevesse, P. Demarque (eds.) Stellar Evolution: What Should Be Done? (Proc. 32nd Liège Intern. Astrophys. Coll.). Univ. de Liège, p.307
 Groenewegen M.A.T., 1993, A&A 271, 180
 Guglielmo F., Epchtein N., Le Bertre T., Fouqué P., Hron J., Kerschbaum F., Lépine J.R.D., 1993, A&AS 99, 31
 Habing H.J., 1996, A&A Rev. 7, 97
 Hacking P., Neugebauer G., Emerson J. et al., 1985, PASP 97, 616
 Han Z., Eggleton P.P., Podsiadlowski P., Tout C.A., 1995, MNRAS 277, 1443
 Haniff C.A., Scholz M., Tuthill P.G., 1995, MNRAS 276, 640
 Herbig G.H., 1965, Kleine Veroff. Remeis-Sternwarte 4, Nr 40, 164
 Herwig F., Blöcker T., Schönberner D., El Eid M., 1997, A&A Letters, in press
 Heske A., 1990, A&A 229, 494
 Hoffmeister C., Richter G., Wenzel W., 1985. Veränderliche Sterne, Springer-Verlag
 Hoffleit D., 1982, The Bright Star Catalogue (4th ed.), Yale University Observatory, New Haven
 Houk N., Cowley A.P., 1975. Michigan Catalogue of Two-Dimensional Spectral Types for the HD stars. Univ. Michigan, Ann Arbor, Vol. 1
 Iben I.Jr., Renzini A., 1983, ARA&A 21, 271
 IRAS Explanatory Supplement, Second Edition, 1988. Joint IRAS Science Working Group, Washington DC, US GPO

- IRAS Point Source Catalogue, Second Edition, 1988. Joint IRAS Science Working Group, Washington DC, US GPO
- IRAS Small-Scale Structure Catalogue, 1985. Joint IRAS Science Working Group, Washington DC, US GPO (SSSC)
- Ivezić Z., Elitzur M., 1995, *ApJ* 445, 415
- Johnson H.R., Ake T.B., Ameen M.M., 1993, *ApJ* 402, 667
- Jorissen A., Mayor M., 1992, *A&A* 260, 115
- Jorissen A., Frayer D.T., Johnson H.R., Mayor M., Smith V.V., 1993, *A&A* 271, 463 (Paper I)
- Jorissen A., Van Eck S., Udry S., Mayor M., 1997, *A&A*, in press
- Jura M., 1988, *ApJS* 66, 33
- Kahane C., Jura M., 1994, *A&A* 290, 183
- Kahane C., Jura M., 1996, *A&A* 310, 952
- Käppeler F., Beer H., Wisshak K., 1989, *Rep. Prog. Phys.* 52, 945
- Keenan P.C., 1954, *ApJ* 120, 484
- Keenan P.C., Boeshaar P.C., 1980, *ApJS* 43, 379
- Keenan P.C., McNeil R.C., 1989, *ApJS* 71, 245
- Kenyon S.J., 1994, *Mem. Soc. Astron. It.* 65, 135
- Kerschbaum F., Olofsson H., Hron J., 1996, *A&A* 311, 273
- Kholopov P.N., Samus' N.N., Frolov M.S., Goransky V.P., Gorynya N.A., Karitskaya E.A., Kazarovets E.V., Kireeva N.N., Kukarkina N.P., Kurochkin N.E., Medvedeva G.I., Pastukhova E.N., Perova N.B., Rastorguev A.S., Shugarov S.Yu., 1985. *General Catalogue of Variable Stars* (4th ed.), Moscow, Nauka (GCVS)
- Knapp G.R., Morris M., 1985, *ApJ* 292, 640
- Knapp G.R., Young K., Lee E., Jorissen A., 1997a, *ApJ*, submitted
- Knapp G.R., Woodhams M.D., Gammie C.F., Young K., Phillips T.G., 1997b, in preparation
- Kolena J., Pataki L., 1977, *AJ* 82, 150
- Lambert D.L., Gustafsson B., Eriksson K., Hinkle K.H., 1986, *ApJS* 62, 373
- Lambert D.L., Smith V.V., Busso M., Gallino R., Straniero O., 1995, *ApJ* 450, 302
- Le Bertre T., 1992, *A&AS* 94, 377
- Lee T.A., 1970, *ApJ* 162, 217
- Levine D.A., et al. 1993. *Infrared Processing and Analysis Center User's Guide* (edition 5), MS 100-22, CalTech, Pasadena
- Lewis B.M., 1989, *AJ* 98, 1814
- Lewis B.M., 1996, *ApJ* 462, 786
- Little S.J., Little-Marenin I.R., Hagen-Bauer W., 1987, *AJ* 94, 981
- Lloyd Evans T., 1983, *MNRAS* 204, 985
- Lloyd Evans T., 1984, *MNRAS* 208, 447
- Lloyd Evans T., 1985. In: Jaschek M., Keenan P.C. (eds.) *Cool Stars with Excesses of Heavy Elements*. Reidel, Dordrecht, p.163
- Lloyd Evans T., Catchpole R.M., 1989, *MNRAS* 237, 219
- Loup C., Forveille T., Omont A., Paul J.F., 1993, *A&A* 99, 291
- Mamon G. A., Glassgold A.E., Huggins P.J., 1988, *ApJ* 328, 797
- Margulis M., van Blerkom D.J., Snell R.L., Kleinmann S.G., 1990, *ApJ* 361, 763
- Mathews G.J., Takahashi K., Ward R.A., Howard W.M., 1986, *ApJ* 302, 410
- McClure R.D., 1983, *ApJ* 268, 264
- McClure R.D., Fletcher J.M., Nemeč J.M., 1980, *ApJ* 238, L35
- Meadows P.J., Good A.R., Wolstencroft R.D., 1987, *MNRAS* 225, 43P
- Merrill P.W., 1922, *ApJ* 56, 457
- Merrill P.W., 1952, *ApJ* 116, 21
- Merrill P.W., 1956, *PASP* 68, 162
- Mendoza V.E., Johnson H.L., 1965, *ApJ* 141, 161
- Mihalas D., Binney J., 1981. *Galactic astronomy* (2nd ed.), W.H. Freeman & co., San Francisco
- Morris M., 1980, *ApJ* 236, 823
- Netzer N., Elitzur M., 1993, *ApJ* 410, 701
- Neugebauer G., Leighton R.B., 1969, *Two-Micron Sky Survey*, NASA SP-3047 (TMSS)
- Noguchi K., Sun J., Wang G., 1991, *PASJ* 43, 311
- Nyman L.-Å., Booth R.S., Carlström U., Habing H.J., Heske A., Sahai R., Stark R., van der Veen W.E.C.J., Winnberg A., 1992, *A&AS* 93, 121
- Nyman L.-Å., Olofsson H., Johansson L.E.B., Booth R.S., Carlström U., Wolstencroft R., 1993, *A&A* 269, 377
- Olson F. M., Raimond E., Neugebauer G., Van Duinen R.J., Habing H.J., 1986, *A&AS* 65, 607
- Olofsson H., Carlström U., Eriksson K., Gustafsson B., Willson L.A., 1990, *A&A* 230, L13
- Olofsson H., Eriksson K., Gustafsson B., Carlström U., 1993, *ApJS* 87, 267
- Omont A., Loup C., Forveille T., te Lintel Hekkert P., Habing H.J., Sivagnanam P., 1993, *A&A* 267, 515
- Patel N.A., Joseph A., Ganesan R., 1992, *J. Astrophys. Astron.* 13, 241
- Petit M., 1982. *Variable Stars*, J. Wiley & Son
- Piccirillo J., *MNRAS* 190, 441
- Price S.D., 1968, *AJ* 73, 431
- Reimers D., 1975, *Mem. Soc. Roy. Sci. Liège*, 6th Ser., 8, 369
- Rouleau F., Martin P.G., 1991, *ApJ* 377, 526
- Rudnitskij G.M., 1976, *Soviet AJ* 20, 693
- Sackmann I.-J., Boothroyd A.I., 1991. In: *Evolution of Stars: The Photospheric Abundance Connection*, G. Michaud & A. Tutukov (eds.) (IAU Symp. 145). Kluwer, Dordrecht, p. 275
- Sahai R., 1992, *A&A* 253, L33
- Sahai R., Liechti S., 1995, *A&A* 293, 198 (SL95)
- Scalo J.M., Ross J.E., 1976, *A&A* 48, 219
- Schaller G., Schaerer G., Meynet G., Maeder A., 1992, *A&AS* 96, 269
- Smith V.V., Lambert D.L., 1988, *ApJ* 333, 219
- Smith V.V., Lambert D.L., 1990, *ApJS* 72, 387
- Stanek K.Z., Knapp G.R., Young K., Phillips T.G., 1995, *ApJS* 100, 169
- Stephenson C.B., 1973, *ApJ* 186, 589
- Stephenson C.B., 1984, *Publ. Warner & Swasey Observ.*, Vol. 3, No. 1 (GCGSS)
- Stephenson C.B., 1989, *Publ. Warner & Swasey Observ.*, Vol. 3, No. 2
- Stephenson C.B., 1990, *AJ* 100, 569
- Tout C.A., Eggleton P.P., 1988, *MNRAS* 231, 823
- Udry S., Mayor M., Van Eck S., Jorissen A., 1997, *A&A*, submitted
- van der Veen W.E.C.J., Habing H.J., 1988, *A&A* 194, 125 (VH)
- Van Eck S., Jorissen A., Mayor M., Udry S., Burnet M., 1997. In: R. Wing (ed.) *The Carbon Star Phenomenon* (IAU Symp. 177). Kluwer, Dordrecht, in press

- van Leeuwen F., Feast M.W., Whitelock P.A., Yudin B., 1997, MNRAS, in press
- Volk K., Cohen M., 1989, AJ 98, 931
- Westerlund B.E., Olander N., 1978, A&AS 32, 401
- Whitelock P., 1994, MNRAS 270, L15
- Willems F.J., de Jong T., 1986, ApJ 309, L39
- Willems F.J., de Jong T., 1988, A&A 196, 173
- Wilson R.E., 1953. A General Catalogue of Stellar Radial Velocities, Carnegie Inst. Washington Publ. 601
- Winfrey S., Barnbaum C., Morris M., Omont A., 1994, BAAS 26, 1382
- Young K., 1995, ApJ 445, 872
- Young K., Phillips T.G., Knapp G.R., 1993a, ApJS 86, 517 (YPK)
- Young K., Phillips T.G., Knapp G.R., 1993b, ApJ 409, 725
- Zuckerman B., Maddalena R.J., 1989, A&A 223, L20

Table 1. IRAS co-added flux densities for S stars, grouped according to their location in the $(K - [12], [25] - [60])$ diagram

Region A: Stellar photospheres

GCGSS	IRAS	F2.2 (Jy)	Ref	F12 (Jy)	F25 (Jy)	F60 (Jy)	F100 (Jy)	Tc	LRS	VC	Sp	Var	P (d)	ΔV (mag)	Name
26	01113+2815	139.4	2	11.95	3.02	0.63		no		F	S3/2				HR 363
79	03377+6303	502.0	2	42.23	10.86	1.82		no	18		S4/2	Lb		0.1	BD Cam, HR 1105
133	05199-0842	92.1	2	7.94	2.06			no	16	S	S4,1				HD 35155
382	07392+1419	331.4	2	25.91	6.51	1.08	0.37		18		M3S	SR		0.2	NZ Gem, HD 61913
729	11098-3209	112.8	2	9.21	2.45	0.39				S	Swk			0.1	NSV 5129, HR 4346
796	12272-4127	207.2	1	17.77	4.47	0.69			18	S	M3-IIIa				NSV 5655, HR 4755
804	13079-8931	167.6	1	15.23	3.88	0.67			17	S	S5,1	Lb:			BQ Oct, HD 110994
826	13372-7136	251.4	1	24.13	6.43	1.08			18	S	S6,2				HD 118685
938	16425-1902	150.1	2	12.24	3.06	^a		no	31	S	Swk				HD 151011
1315	22521+1640	283.4	2	27.58	7.33	1.23	0.67	yes		S	S4/1	SRb	50	0.3	HR Peg, HR 8714
1322	23070+0824	938.4	2	84.67	20.31	3.20	0.96	no	18		M4S	SRa	93	0.3	GZ Peg, 57 Peg

a: Strong cirrus contamination

Region B: Small ZrO index and no [25] - [60] excess

GCGSS	IRAS	F2.2 (Jy)	Ref	F12 (Jy)	F25 (Jy)	F60 (Jy)	F100 (Jy)	Tc	LRS	VC	Sp	Var	P (d)	ΔV (mag)	Name	
8	00192-2020	1356.0	2	199.1	81.66	14.57+	6.08+	yes	16		M5-6Se	SRc	159	1.9	T Cet	
134	05208-0436	80.2	8	20.56	10.85	1.65			43	U	M4Swk				V535 Ori	
168	05495+1547	26.1	1	11.35	3.52	0.62				F	S7.5,1e	M	494	4.9	Z Tau	
221	06266-1148	27.6	7							F	S-*2e					
		JD 2 445 420:		8.97	4.10	0.94										
		JD 2 445 620:		14.57	7.64	1.14										
265	06466-2022	87.2	2	8.34	2.41	0.47			16		M4S				HD 49683	
323	07117-1430	40.6	2	4.17	1.52	0.30										
408	07461-3705			14.11	6.25	0.87			14	F	S6*1					
436	07545-4400	51.6	1						22	E	S4,2	M	340	4.7	SU Pup	
		JD 2 445 470:		15.44	6.88	1.29										
		JD 2 445 645:		25.03	11.95	1.96										
446	07573-6509	27.6	1	5.45	1.72	0.27					S7,2	M	280	2.7	X Vol	
474	08098-2809	55.5	2	7.07	2.23	0.42				S	S4,2				-27:5131	
533	08348-3617	55.5	1	11.25	3.44	0.53			18	S	S5,2				-36:4827	
589	09076+3110	2808.0	2	489.88	210.29	34.57+	11.71+	yes	22		M6S	SRc	120	1.5	RS Cnc(OH?)	
626	09411-1820			10.0	4.10	0.71				F	M0S	M	300	5.0	FM Hya	
704	10436-3459	133.2	1	31.32	13.98	1.93	1.09		42	E	S5,4	SR	104	2.0	Z Ant	
903	15492+4837	1295.0	2	205.41	98.75	17.13+	7.14+	yes	41		M6.5S	SRb	148	1.5	ST Her	
914	16097-6158			12.24	4.51	0.70				F	S4,1	M	323	5.0	Y TrA	
948	16552-5335	39.1	1	8.80	2.90						S4,4					
1099	19008+1210	105.8	2	11.54	3.62				yes	S	S5/2	Lb		0.6	V915 Aql	
1131	19226-2012	20.5	7	7.32	2.94	0.50				F	M8Swk	M	332	7.0	TT Sgr	
1165	19486+3247	5813.	2						yes	E	S7/1.5e	M	408	6.	χ Cyg (SiO)	
		JD 2 445 450:		1781.65 ^a	552.84	95.47+	21.32									
		JD 2 445 640:		1215.31 ^a	414.40	71.64+	14.50									
1211	20213+0047	152.9	2	22.54	7.27	1.29			17	S	S7,2	M	364	4.5	V865 Aql	
1346	23595-1457	120.3	2	13.11	3.88	0.73			yes	16	F	S5-7/1.5-3e	M	351	7.7	W Cet

a: detector probably saturated

+: the 'zero-crossing' flux density F_z has been adopted instead of the template flux density F_t , indicating a possibly resolved shell (see Sect. 2.2)

Table 1. Continued.

Region C: [12] – [25] and [25] – [60] excesses, silicate emission common

CGCSS	IRAS	F2.2 (Jy)	Ref	F12 (Jy)	F25 (Jy)	F60 (Jy)	F100 (Jy)	Tc	LRS	VC	Sp	Var	<i>P</i> (d)	ΔV (mag)	Name
6	00135+4644	37.4	2	15.96	6.24	1.57	0.85		16	F	S4/7e	M	346	6.9	X And
9	00213+3817	453.3	2	335.74	175.66	26.41+	9.45	yes		E	S5-7/4-5e	M	409	9.1	R And (SiO)
14	00445+3224	96.5	2	37.75	18.58	3.97	2.10		22	F	S6/2e	M	430	7.8	RW And
28	01159+7220	147.4	2	343.76	192.52	30.14+	10.88		22	E	S4,6e	M	612	8.2	S Cas (SiO)
36	01266+5035	34.1	6	6.59	1.93	0.45					S6/8e	M	355	5.3	RZ Per
49	02143+4404	275.7	2	166.42	70.94	14.01	5.43	yes	22	E	S7/1e	M	396	7.9	W And (SiO)
149	05374+3153	280.8	2	45.33	23.32	5.00		yes	43		M2S	Lc		0.2	NO Aur
231	06331+1415	136.9	2	21.95	10.35	2.61 ^a	3.90	no	42	F	S8,5	SRa	1145	1.4	DY Gem
283	06571+5524	118.1	2						16	F	S5/5e	M	378	7.1	R Lyn (SiO)
		JD 2 445 420:		17.55	5.61	1.25									
		JD 2 445 620:		28.46	9.46	2.01									
307	07043+2246	88.0	2					yes	16	F	S3,9e	M	370	8.0	R Gem
		JD 2 445 435:		22.23	7.53	2.21	1.40								
		JD 2 445 620:		42.33	16.81	3.73	1.48								
316	07092+0735			12.23	5.63	1.06	0.36			E	Se	M	420	4.8	WX CMi
326	07149+0111	70.5	2						16		M7se:	M	395	7.4	RR Mon
		JD 2 445 440:		27.76	11.75	2.31	0.85								
		JD 2 445 625:		15.77	7.21	1.69	1.03								
341	07197–1451			20.24	10.47	1.86			27	E		M	314	4.0	TT CMa
347	07245+4605	964.7	2	133.50	65.92	13.20+ ^d	5.58+	yes	23		M6S	SRc	110	2.5	Y Lyn (SiO)
614	09338–5349	68.0	1						01	E	S7,8e	M	408	3.0	UU Vel
		JD 2 445 510:		11.53	5.98	1.77									
		JD 2 445 580:		17.79	9.37										
649	09564–5837			156.15	71.37	14.31			15	E	S6.5/1-	SRb	109	1.3	RR Car
656	10017–7012	43.7	1	6.02	1.72	0.37					S5,6	M		3.5	KN Car
816	13136–4426	356.8	1	56.55	20.77	4.04	1.78		43	C	S6/8=CS	SR	114	2.0	UY Cen
821	13240–5742			13.40	6.27				14	F	S6*3	SR	198	1.9	EE Cen
861	14372–6106	43.3	9	21.38	9.13				15	E					CSV2170
872	15030–4116	111.8	1	21.81	9.23	2.18				F	S7,8e	M	326	5.6	GI Lup
931	16334–3107	377.0	2	52.49	21.88	4.22 ^c		^b	16	E	S8/4var	SRa	194	3.5	ST Sco
954	17001–3651	453.3	1						22	E	S7,2	M	449	8.2	RT Sco
		JD 2 445 410:		170.65	69.64	15.37									
		JD 2 445 600:		269.51	118.53	25.01									
–	17081+6422	377.0	2	61.96	25.52	4.87	2.27					Lb		0.4	TV Dra
1093	18575–0139	37.7	1	17.18	5.92	1.83					SC	M:		3.8	VX Aql
1096	18586–1249	242.3	2	51.78	19.19	4.03			21	E	S6/3e	M	395	8.8	ST Sgr
1112	19111+2555	18.7	6						41		SC	M	438	5.8	S Lyr
		JD 2 445 440:		43.81	21.43	4.39									
		JD 2 445 630:		84.17	38.23	7.53	2.73								
1115	19126–0708	286.0	2						22	E	S6/6e	M	490	7.0	W Aql (SiO)
		JD 2 445 440:		1397.52 ^e	719.87	132.67+	36.87								
		JD 2 445 630:		1057.16 ^e	481.93	100.58+	24.90								
1117	19133–1703	166.1	2	42.27	14.62	4.76+	4.76+	yes		F	S5/6e	M	394	5.8	T Sgr
1150	19354+5005	107.7	2	107.44	52.86	12.22+	5.52	yes	22	E	S6/6e	M	426	8.3	R Cyg (SiO)
1159	19451+0827	15.3	7	7.69	3.53	0.84				I	Se	M	607	2.0	QU Aql
1175	19545–1122			7.59	3.80				29	E	M6S				V1407 Aql

a: close weak source

b: profile badly distorted by close source

c: close weak source apparent on some scans

d: moves to Region B after removing the extended shell contribution

e: Detector possibly saturated

+–: the ‘zero-crossing’ flux density F_z has been adopted instead of the template flux density F_t , indicating a possibly resolved shell (see Sect. 2.2)

Table 1. Region C (continued)

GCGSS	IRAS	F2.2 (Jy)	Ref	F12 (Jy)	F25 (Jy)	F60 (Jy)	F100 (Jy)	Tc	LRS	VC	Sp	Var	P (d)	ΔV (mag)	Name	
1200	20114+7702										I	S5/6e	M	326	6.9	SZ Cep
			JD 2 445 394:	7.27	2.71	0.68										
			JD 2 445 580:	9.67	3.45	0.72										
1268	21172-4819	14.9	1	7.15	2.34	0.63					I	S2,5				-48:13866
C3107 ^a	22036+3315	44.1	2	15.92	7.28	1.60					C	SC	M	439	6	RZ Peg
1294	22196-4612	4211.	1					yes	42	E	S5,7	SRb	150	1.3	π^1 Gru	
			JD 2 445 470:	969.23	471.63	88.71+	23.88									
			JD 2 445 645:	1421.10 ^b	419.22	92.25+	25.80									
1345	23554+5612	66.7	2	52.07	28.10	8.80	5.28		42	E	S6/6e	M	476	6.9	WY Cas	
1347	00001+4826	18.2	6	50.54	24.54	4.15			21	E	S5/6e	M	396	3.3	IW Cas	

a: Star number from the *General Catalogue of Carbon Stars* (Stephenson 1989)

b: Detector possibly saturated

+: the ‘zero-crossing’ flux density F_z has been adopted instead of the template flux density F_t , indicating a possibly resolved shell (see Sect. 2.2)

Table 1. Continued.Region D: No silicate emission, weak $K - [12]$ excess, some $[25] - [60]$ excess

CGCSS	IRAS	F2.2 (Jy)	Ref	F12 (Jy)	F25 (Jy)	F60 (Jy)	F100 (Jy)	Tc	LRS	VC	Sp	Var	P (d)	ΔV (mag)	Name
12	00435+4758	64.9	2	8.47	2.49	^a	^a	yes	01	S	S5/3e	M	277	7.7	U Cas
17	00486+3406	36.3	5	4.56	1.44	0.35					S6/3e	M	328	7.2	RR And
20	00578+5620	169.2	2	21.87	7.81	2.43			16	F	S6/3	SRb	136	1.8	V365 Cas
29	01186+6634	46.6	2	5.10	1.90	0.42									
57	02228+3753	95.6	2	9.89	2.80	0.66+	0.70		01	S	S8,8	SR	159	1.1	BI And
103	04352+6602	398.5	2	42.56	11.64	3.70	2.21	yes	17	S	S4,7e	M	373	7.1	T Cam
116	04543+4829	175.5	2	12.81	4.27	1.38		yes		F	S5,8	SRb	182	0.7	TV Aur
160	05440+1753			4.72	1.55	0.50						SRa	364	2.5	EI Tau
237	06347+0057	51.1	2	6.18	2.21	0.85						Lb		0.9	CX Mon
312	07095+6853	138.2	2	14.57	5.98	1.94+	1.87	yes			M5S	Lb		0.6	AA Cam
387	07399-1045	177.2	2	19.48	7.25	2.08			18	S	S3,6	SRb		2.8	SU Mon
524	08308-1748	65.5	2	5.85	2.00	^a						M	250	1.5	SZ Pyx
556	08461-7051	53.0	1	5.70	1.49	0.46	0.33				SC	Lb:		0.4	UX Vol
617	09358-6536	39.5	1	4.00	1.22	0.27					S7,8				
696	10389-5149	109.7	1	10.61	3.21	1.11			18	S	S5,2	Lb		0.4	HP Vel
787	12135-5600			19.78	6.55	1.65			18		SC6/8e	M		4.3	BH Cru
803	12417+6121	39.5	3	4.39	1.38	0.35	0.39	yes			S3/6e	M	226	5.6	S UMa
830	13440-5306	129.5	1	15.60	5.66	2.08			18		SC	Lb		1.2	AM Cen
834	13477-6009	387.6	1	49.16	14.57	3.42			17	S	S8,5	SR	307	3.3	VX Cen
904	15548-7420	58.1	1	6.12	1.93	0.65	0.59				SC	SRa	152	3.5	VY Aps
923	16209-2808	71.2	2	7.71	4.10	1.27									
940	16472-6056	49.2	1	5.71	2.06	0.72					SC	M:		2.3	LQ Ara
978	17206-2826	319.4	2	39.93	11.48	2.72			17	S	S5,4	SRb	320	1.4	V521 Oph
	17553+4521	545.0	2	55.41	17.50	4.14+ ^d	3.20+	yes	17		MII-III	SRb	120	0.9	OP Her
1011	17562-1133			8.45	3.30	^c			01						
1056	18310-3541	53.0	7	5.99	2.05	0.62					S5,4	L		0.5	V3574 Sgr
1141	19311+2332	258.2	2	32.48	13.87	3.06			16	F	S6/5	Lb		3.7	EP Vul (SiO)
1188	20026+3640	356.8	2	40.22	15.45	5.37		yes	31	S	S7,5	SRb	212	3.0	AA Cyg
1310	22479+5923	91.3	2	10.03	3.25	^a				F	S6/2	SRb	60	1.4	CV Cep
1308	22476+4047	766.3	2	100.51	32.66	10.25+	10.07+		16	S	S7.5/1	SRb	174	1.7	RX Lac
1339	23380+7009	60.9	2	7.95	2.89	0.86				F	M6S				S1339

a: profile badly distorted by close source

c: strong cirrus contamination

d: moves to Region B after removing the extended shell contribution

+: the 'zero-crossing' flux density F_z has been adopted instead of the template flux density F_t , indicating a possibly resolved shell (see Sect. 2.2)

Table 1. Continued.

Region E: Strong [25] – [60] excess, many resolved shells

CGCSS	IRAS	F2.2 (Jy)	Ref	F12 (Jy)	F25 (Jy)	F60 (Jy)	F100 (Jy)	Tc	LRS	VC	Sp	Var	P (d)	ΔV (mag)	Name
82	03452+5301	66.7	2	7.66	3.36	2.40 ^b			01	F	S5,8	Lb		0.8	WX Cam
89	04123+2357	258.5	2	25.13	7.63	3.30+	2.56	yes		S					+23:654
114	04497+1410	1010.	2	87.25	22.19	7.52+	3.57	yes	18		S3,1	SRb	30	0.2	σ^1 Ori
117	04599+1514	88.8	2	11.11	3.45	1.44			17		SC	SRb	370	1.1	GP Ori
212	06197+0327	144.7	2	17.16	4.63	2.66+	5.88+		18	S	SC	SR	310	1.1	FU Mon
422	07507–1129	79.5	2	7.21	1.82	0.48		yes		I	S5/2	Lb		0.1	NQ Pup
540	08388–5116	3.9	1	5.39	2.02	0.97					S6,8				S325
652	10015–4634	58.7	1	6.31	1.84	1.23					S5,8				
817	13163–6031	94.7	1	21.52	12.91	7.01					SC5:/8				TT Cen
929	16316–5026	71.2	8						42		Se				
	JD 2 445 380:	65.34		31.24	16.70+	30.18+									
	JD 2 445 600:	98.46		45.58	20.72+	38.74+									
1189	20044+2417	129.5	2	19.16	7.55	4.95+	7.30+		16	F	S4,2	SRa	370	2.0	DK Vul
1195	20100–6225	133.2	1	11.03	2.82	1.77+	3.27+	yes	18	S	S4,4				HD 191630
1196	20120–4433	187.2	1	39.13	25.58	13.35+	25.88+		16	F	S4,4	SRb	223	2.6	RZ Sgr

b: close weak source apparent on some scans

+: the ‘zero-crossing’ flux density F_z has been adopted instead of the template flux density F_t , indicating a possibly resolved shell (see Sect. 2.2)

Table 2. S stars whose circumstellar envelopes are resolved at 60 μm , listed according to the region to which they belong in the $(K - [12], [25] - [60])$ diagram (see Fig. 3). In column Rem, YPK+ and YPK- denote stars found to be extended or not, respectively, by Young et al. (1993a). Stars with no YPK label were not examined by Young et al. (1993a). The mass loss rates and wind velocities listed in columns \dot{M} and V_e , respectively, are taken from Table 6

IRAS	Name	Var	F60 (Jy)	F_z/F_p	W25 (')	W50 (')	QF	\dot{M} ($M_\odot \text{ y}^{-1}$)	V_e (km s^{-1})	Rem.
Region B										
00192-2020	T Cet	SRc	14.6	1.05	1.96	1.44	14.5	4.0(-8) ^a	6.9	YPK-,b
19486+3247	χ Cyg	M						3.5(-7)	9.5	YPK+,f
	JD 2 445 450:		95.5	1.01	1.96	1.45	9.5			
	JD 2 445 640:		71.6	1.002	1.93	1.42	0.4			
09076+3110	RS Cnc	SRc	34.6	1.04	1.97	1.44	29.2	1.7(-7)	7.4	YPK+,b,f
	RS Cnc							4.5(-8)	2.6	e
15492+4837	ST Her	SRb	17.1	1.02	1.95	1.43	6.7	1.7(-7)	9.5	YPK+,b
Region C										
00213+3817	R And	M	26.4	1.05	2.01	1.47	30.6	7.5(-7)	9.3	YPK-
01159+7220	S Cas	M	30.1	1.01	1.94	1.42	10.4	3.5(-6)	20.0	YPK-
07245+4605	Y Lyn	SRc	13.2	1.15	2.00	1.45	30.9	2.0(-7)	8.6	YPK+,d
19126-0708	W Aql	M						1.1(-5)	18.7	YPK-
	JD 2 445 440:		132.7	1.006	1.93	1.44	5.8			
	JD 2 445 630:		100.6	1.02	1.95	1.44	7.5			
19133-1703	T Sgr	M	4.8	1.11	2.05	1.48	8.0	3.5(-7)	14.1	b
19354+5005	R Cyg	M	12.2	1.03	1.96	1.44	10.0	1.5(-6)	10.5	YPK+,f
22196-4612	π^1 Gru	SRb						4.0(-7)	11.0	YPK+,f
	JD 2 445 470:		88.7	1.04	1.98	1.44	37.9			
	JD 2 445 645:		92.2	1.07	2.02	1.49	38.3			
Region D										
02228+3753	BI And	SR	0.7	-	2.17	1.58	2.6			
07095+6853	AA Cam	Lb	1.9	-	2.08	1.57	4.1	2.5(-7)	17.9	
17553+4521	OP Her	SRb	4.1	1.15	2.16	1.53	42.4			b
22476+4047	RX Lac	SRb	10.2	1.16	2.11	1.52	23.6	1.5(-8)	3.4	b
Region E										
04123+2357	BD+23°654	-	3.3	1.20	2.18	1.53	7.2			
04497+1410	σ^1 Ori	SRb	7.5	1.48	2.89	1.71	34.8	< 4.0(-8)		c
06197+0327	FU Mon	SR	2.7	1.40	2.42	1.62	12.6	9.0(-8)	2.8	b
16316-5026	S929	-								
	JD 2 445 380:		16.7	1.50	3.08	1.81	24.8			b
	JD 2 445 600:		20.7	1.89	-	1.87	24.1			b
20044+2417	DK Vul	SRa	4.9	1.22	2.32	1.60	25.3	2.5(-7)	5.0	b
20100-6225	HD 191630	-	1.8	1.35	2.57	1.67	24.0	< 9.0(-7)		b,c
20120-4433	RZ Sgr	SRb	13.3	1.26	2.28	1.58	62.1	1.8(-6)	8.8	YPK+,b,d

Notes:

a: numbers between parentheses refer to power of ten

b: 100 μm profile wider than point-source template

c: listed as extended at 60 μm in the IRAS *Small Scale Structure Catalogue*

d: listed as extended at 100 μm in the IRAS *Small Scale Structure Catalogue*

e: two-components wind

f: circumstellar shell resolved in CO (Sahai 1992; Stanek et al. 1995)

Table 3. Masers in S stars

Star	IRAS	SiO	H ₂ O	OH	Refs
Region A					
BD Cam	03377+6303	-	N	-	B96
NZ Gem	07392+1419	-	N	-	B96
HR Peg	22521+1640	N	N	-	B96, Z89
GZ Peg	23070+0824	N	N	-	D73, H89
Region B					
T Cet	00192-2020	N	N	N	A89a, A90, D76, H94, L78, P71
V535 Ori	05208-0436	-	N	N	D89, H91
Z Tau	05495+1549	N	-	N	B78, J91
RS Cnc	09076+3110	N	N	Y?	D73, D76, A92, D82, K77, L78, L90, P92, R76
Z Ant	10436-3459	-	-	N	H91
ST Her	15492+4837	-	N	N	D73, D76, D82, P79
S Her	16496+1501	N	N	-	B77a, B84, B87, B90, E88, S81
χ Cyg	19486+3249	Y	N	N	A89b, A92, B87, B94, C83a, C96, D76, J84, J85, J87, J91, N85, O85, P92
W Cet	23595-1457	N	N	-	B77a, B84, L76, L78
Region C					
R And	00213+3817	Y	N	N	B77a, B78, B87, B94, B96, C96, D78, F75, J91, T94
RW And	00445+3224	N	N	N	B77a, B78, C83b, C96, F75, F78, K77, W72
S Cas	01159+7220	Y	N	N	B77a, B94, F73, T94
RZ Per	01266+5035	N	-	-	B77a
W And	02143+4404	Y	N	N	A89b, B77a, B87, B94, C96, D96, D78, K77, O80, T94, W72
NO Aur	05374+3153	-	N	N	B75, B81, B96
R Lyn	06571+5524	Y	N	-	B77a, B94, K84, S81
R Gem	07043+2246	N	N	N	B77a, B78, B96, J91, L78, W72
RR Mon	07149+0111	N	-	N	K77, L78
TT CMa	07197-1451	N	N	N	B90, B96, H91
Y Lyn	07245+4605	Y	N	N	A90, B75, B81, D73, D82
RR Car	09564-5837	N	N	-	H94, L77
ST Sco	16334-3107	N	N	N	B77a, B94, J88, L77, W72
RT Sco	17001-3651	N	N	N	B77b, C71, L76, L77, L78, S88

Table 3. Masers in S stars (Continued)

Star	IRAS	SiO	H ₂ O	OH	Refs
Region C (continued)					
TV Dra	17081+6422	N	-	N	B94, W72
ST Sgr	18586-1249	N	N	-	B77a
W Aql	19126-0708	Y	N	N	B77a, B84, B87, B94, D89, L78, W72, Z79
T Sgr	19133-1703	N	N	-	B77a, B90
R Cyg	19354+5005	Y	N	N	B94, B96, C96, P92, W72, Z79
RZ Peg	22036+3315	-	N	-	B96
π^1 Gru	22196-4612	N	N	-	D89, H90
WY Cas	23554+5612	-	N	-	B77a, C83b
Region D					
U Cas	00435+4758	N	N	-	B77a, C83b, J91, S81
RR And	00486+3406	N	N	N	B77a, F78
S29	01186+6634	-	N	-	C83b
BI And	02228+3753	-	N	-	C83b
T Cam	04352+6602	N	N	-	B77a, B94, D76, J91
TV Aur	04543+4829	N	-	-	B77a, B94
EI Tau	05440+1753	N	-	-	B77a
AA Cam	07095+6853	-	N	-	B96
SU Mon	07399-1045	N	-	-	B94
SZ Pyx	08308-1748	-	N	-	C83b
S UMa	12417+6121	N	N	-	B77a, B96, D78
VX Cen	13477-6009	N	-	-	P92
OP Her	17553+4521	-	N	-	B96
EP Vul	19311+2332	Y	-	N	B94, R76
AA Cyg	20026+3640	N	N	-	B77a, B94, B96, D82
RX Lac	22476+4047	-	N	N	D73, D82, W72
Region E					
o^1 Ori	04497+1410	-	N	N	B96, D73, P71
GP Ori	04599+1514	N	-	-	L78
FU Mon	06197+0327	N	-	-	B77a
RZ Sgr	20120-4433	-	-	N	C71

References to Table 3. The parentheses at the end of each reference indicate which maser is probed by the paper

-
- A89a: Allen D.A., Hall P.J., Norris R.P., Troup E.R., Wark R.M., Wright A. E., 1989, MNRAS 236, 363 (SiO)
A89b: Alcolea J., Bujarrabal V., Gallego J. D., 1989, A&A 211, 187 (SiO)
A90: Alcolea J., Bujarrabal V., Gomez-Gonzalez J., 1990, A&A 231, 431 (SiO)
A92: Alcolea J., Bujarrabal V., 1992, A&A 253, 475 (SiO)
B75: Bowers P.F., 1975, AJ 80, 512 (OH)
B77a: Blair G.N., Dickinson D.F., 1977, ApJ 215, 552 (SiO, H₂O)
B77b: Bowers P.F., Kerr F.J., 1977, A&A 57, 115 (OH)
B78: Bowers P.F., Sinha R.P., 1978, AJ 83, 955 (OH)
B81: Bowers P.F., 1981, AJ 86, 1930 (OH)
B84: Bowers P.F., Hagen W., 1984, ApJ 285, 637 (H₂O)
B87: Bujarrabal V., Planeses P., del Romero A., 1987, A&A 175, 164 (SiO)
B90: Benson P.J., Little-Marenin I.R., Woods T.C., Attridge J.M., Blais K.A., Rudolph D.B., Rubiera M.E., Keefe H.L., 1990, ApJS 74, 911 (SiO, H₂O, OH)
B94: Biegging J.H., Latter W.B., 1994, A&A 422, 765 (SiO)
B96: Benson P.J., Little-Marenin I.R., 1996, ApJS 106, 579 (H₂O)
C71: Caswell J.L., Robinson B.J., Dickel H.R., 1971, Ap. Letters 9, 61 (OH)
C83a: Clemens D.P., Lane A.P., 1983, ApJ 266, L117 (SiO)
C83b: Crocker D.A., Hagen W., 1983, A&AS 54, 405 (H₂O)
C96: Cho S.H., Kaifu N., Ukita N., 1996, A&AS 115, 117 (SiO)
D73: Dickinson D.F., Bechis K.P., Barrett, A.H., 1973, ApJ 180, 831 (H₂O)
D76: Dickinson D.F., 1976, ApJS 30, 259 (H₂O)
D78: Dickinson D.F., Snyder L.E., Brown L.W., Buhl D., 1978, AJ 83, 36 (SiO)
D82: Dickinson D.F., Dinger A.S., 1982, ApJ 254, 136 (H₂O)
D89: Deguchi S., Nakada Y., Forster J.R., 1989, MNRAS 239, 825 (H₂O)
E88: Engels D., Schmid-Burgk J., Walmsley C.M., 1988, A&A 191, 283
F73: Fillit R., Foy R., Gheudin M., 1973, Ap. Letters 14, 135 (OH)
F75: Foy R., Heck A., Mennessier M.O., 1975, A&A 43, 175 (OH)
F78: Fix J.D., Weisberg J.M., 1978, ApJ 220, 836 (OH)
H89: Heske A., 1989, A&A 208, 77 (SiO)
H90: Haikala L.K., 1990, A&AS 85, 875 (SiO)
H91: te Lintel Hekkert P., Caswell J.S., Habing H.J., Haynes R.F., Norris R.P., 1991, A&AS 90, 327 (OH)
H94: Haikala L.K., Nyman L.A., Forsstrom V., 1994, A&AS 103, 107 (SiO)
J84: Jewell P.R., Batrla W., Walmsley C.M., Wilson T.L., 1984, A&A 130, L1 (SiO)
J85: Jewell P.R., Walmsley C.M., Wilson T.L., Snyder L.E., 1985, ApJ 298, L55 (SiO)
J87: Jewell P.R., Dickinson D.F., Snyder L.E., Clemens D.P., 1987, ApJ 323, 749 (SiO)
J91: Jewell P.R., Snyder L.E., Walmsley C.M., Wilson T.L., Gensheimer P.D., 1991, A&A 242, 211 (SiO)
K77: Kolena J., Pataki L., 1977, AJ 82, 150 (OH)
-

References to Table 3 (continued).

- K84: Kuiper T.B.H., Swanson P.N., Dickinson D.F., Rodríguez Kuiper E.N., Zimmermann P., 1984, ApJ 286, 310 (H₂O)
L76: Lépine J.R.D., Paes de Barros M.H., Gammon R.H., 1976, A&A 48, 269 (H₂O)
L77: Lépine J.R.D., Paes de Barros M.H., 1977, A&A 56, 219 (H₂O)
L78: Lépine J.R.D., Le Squeren A.M., Scalise E., 1978, ApJ 225, 869 (SiO)
L90: Lewis B.M., Eder J., Terzian Y., 1990, ApJ 362, 634 (OH)
N85: Nyman L.A., Olofsson H., 1985, A&A 147, 309 (SiO)
O80: Olon F.M., Winnberg A., Matthews H. E., Schultz G.V., 1980, A&AS 42, 119 (OH, H₂O)
O95: Olofsson H., Rydbeck O.E.H., Nyman L.A., 1985, A&A 150, 169 (SiO)
P71: Pashchenko M.I., Slysh V., Strukov I., Fillit R., Gheudin M., Nguyen-Quang-Rieu, 1971, A&A 11, 482 (OH)
P79: Pashchenko M.I., Rudnitskij G.M., 1979, Astron. Tsirk. 1040, 4
P92: Patel N.A., Joseph A., Ganesan R., 1992, J. Astron. Astrophys. 13, 241 (SiO)
R76: Rudnitskij G.M., 1976, Soviet AJ 20, 693 (OH)
S81: Spencer J.H., Winnberg A., Olon F.M., Schwartz P.R., Matthews H.E., Downes D., 1981, AJ 86, 392 (SiO)
S88: Sivagnanam P., Le Squeren A.M., Foy R., 1988, A&A 206, 285 (OH)
T94: Takaba H., Ukita N., Miyaji T., Miyoshi M., 1994, PASJ 46, 629 (H₂O)
W72: Wilson W.J., Barrett A.H., 1972, A&A 17, 385 (OH)
Z79: Zuckerman B., 1979, ApJ 230, 442 (SiO)
-

Table 4. S stars observed in CO at the Caltech Submillimeter Observatory

GCGSS	Other	$\alpha(1950)$	$\delta(1950)$	l	b	SpT	Var	P (d)	V_{LSR} (km s^{-1})	r.m.s. (mK)
89	HD 26816	04 12 23.7	+23 57 15	171.6	-19.0	S	Lb :	-	-	17
117	GP Ori	04 59 56.7	+15 14 58	186.0	-15.7	SC7/8	SRb	370 :	+86, +92	37
149	NO Aur	05 37 26.8	+31 53 43	176.9	+0.7	M2IIIS	Lc	-	-7, -3	13
212	FU Mon	06 19 46.1	+03 27 00	206.6	-4.9	SC	SR	310	-46, -39	10
283	R Lyn	06 57 10.8	+55 24 06	161.2	+23.4	S5/5e	Mira	378	+9, +28	18
422	NQ Pup	07 50 43.6	-11 29 41	230.5	+8.04	S5/2	Lb	-	-	42
589	RS Cnc	09 07 37.8	+31 10 03	194.5	+42.1	M6IIIaSe	SRc?	120	+7, +11	23
626	FM Hya	09 41 10.3	-18 20 43	252.8	+25.5	M0S	Mira	300	-	17
704	Z Ant	10 43 40.2	-34 59 17	275.9	+20.9	S5, 4	SR	104	-	10
796	HR 4755	12 27 16.8	-41 27 35	298.6	+21.0	M2II - III	-	-	-2	10
803	S UMa	12 41 45.5	+61 22 00	124.6	+56.0	S3/6e	Mira	226	+5, +18	10
816	UY Cen	13 13 36.8	-44 26 27	307.6	+17.9	S6/8, CS	SR	114	-23	39

Notes to Table 4:

1. The spectral type in column 8 is from the GCGSS
2. Column 10 gives the observed range of optical velocities, taken from the following references: Brown et al. 1990 (GCGSS 149 and 589), Udry et al. (1997) and Jorissen et al. (1997) (GCGSS 117 and 212), Wilson 1953 (GCGSS 283, 803 and 816), Hoffleit (1982) (GCGSS 796)
3. All stars observed in the CO(2-1) line except GP Ori, NQ Pup and UY Cen, which were observed in the CO(3-2) line

Table 5. CO(2–1) data for the four S stars detected by the CSO observations

GCGSS		I_{CO} ($\text{K} \times \text{km s}^{-1}$)	T(peak) (K)	V_c (km s^{-1})	V_e (km s^{-1})
212	FU Mon	0.63 ± 0.05	0.15 ± 0.02	-41.7 ± 0.2	2.8 ± 0.3
283	R Lyn	0.89 ± 0.19	0.08 ± 0.02	$+15.7 \pm 1.4$	9.3 ± 1.7
589	RS Cnc	13.3 ± 0.9	0.78	+7.7	7.4
			1.17	+6.8	2.6
704	Z Ant	0.73 ± 0.09	0.07 ± 0.02	-15.6 ± 1.0	7.4 ± 1.3

Table 6. A compilation of CO data for S stars (columns 3–10; for data prior to 1990, see Loup et al. 1993) and mass loss rates fitting these data (columns 11–19), assuming $T_\star = 2500$ K, $R_\star = 2.5 \times 10^{13}$ cm, and $f = n(\text{CO})/n(\text{H}_2) = 6.5 \times 10^{-4}$

IRAS	Star	Observations								Model								
		Line	HPBW "	rms (K)	I_{CO} (K km/s)	T_{MB} (K)	V_c (km/s)	V_e (km/s)	Ref	D (pc)	V_e (km/s)	dM/dt ($M_\odot \text{ yr}^{-1}$)	radius (cm) (")	Line	HPBW (")	T_{MB} (K)	I_{CO} (K km/s)	
Region A:																		
03377+6303	BD Cam	1–0	50	0.02	–	–	–	–	BL94	92	(8.5)	$< 1.6 \times 10^{-8}$						
		2–1	13	0.05	–	–	–	–	SL95									
12272–4127	HR 4755	2–1	30	0.01	–	–	–	–	this work	145	(8.5)	$< 2.3 \times 10^{-8}$						
13372–7136	GCGSS 826	1–0	45	0.01	–	–	–	–	SL95	130	(8.5)	$< 5.8 \times 10^{-8}$						
22521+1640	HR Peg	1–0	50	0.01	–	–	–	–	BL94	125	(8.5)	$< 6.3 \times 10^{-8}$						
Region B:																		
00192–2020	T Cet	1–0	100	0.14	–	–	–	–	K97									
		2–1	30	0.05	2.6	0.28	+23.9	6.9	K97	130	6.9	4.6×10^{-8}	1.26×10^{16}	6.5	2–1	30	0.24	3.32
*09076+3110	RS Cnc	1–0	33	0.07	7.3	0.77	+7.5	7.0	N92									
		2–1	30	0.02	13.3	0.78	+7.7	7.4	this work	200	7.4	1.9×10^{-7}	2.61×10^{16}	8.7	2–1	30	0.79	10.63
		2–1	30			1.17	+6.8	2.6	this work									
		3–2	20	0.07	29.8	4.3	+6.8	4.8	S95									
		3–2	20	0.07	21.9	2.63	+6.8	5.8	K97									
09410–1820	FM Hya	2–1	30	0.02	–	–	–	–	this work	1800	(8.5)	$< 1.0 \times 10^{-6}$						
10436–3459	Z Ant	2–1	30	0.01	0.73	0.07	–15.6	7.4	this work	900	7.4	2.9×10^{-7}	3.26×10^{16}	2.4	2–1	30	0.07	0.84
15492+4837	ST Her	1–0	22	–	4.9	0.24	–5.3	8.6	KJ94	290	9.5	2.0×10^{-7}	2.43×10^{16}	5.6	1–0	22	0.17	3.47
		2–1	13	–	17.4	1.05	–4.6	8.8	KJ94						2–1	13	1.12	20.50
		2–1	13	0.10	–	0.45	–4.4	9.1	SL95									
		3–2	20	0.07	5.1	0.34	–4.4	12.0	K97					3–2	20	0.41	9.1	
19486+3247	χ Cyg	1–0	23	0.10	–	2.20	+9.6	10.2	H90	106	9.5	2.6×10^{-7}	2.85×10^{16}	18	1–0	23	1.68	37.79
		1–0	45	–	10.6	–	+10	10	M90						1–0	45	0.68	13.45
		1–0	50	0.02	11.8	0.77	+9.7	8.9	BL94						1–0	50	0.57	11.14
		1–0	100	0.07	3.6	0.27	+9.7	10.1	K97						1–0	100	0.16	3.00
		2–1	13	0.24	–	6.2	+10.0	8.8	SL95						2–1	13	5.47	105.2
		2–1	25	0.03	25.4	1.77	+9.9	9.0	BL94						2–1	25	2.45	43.76
		2–1	30	0.15	22.7	1.63	+9.9	9.9	K97						2–1	30	1.85	32.59
		3–2	20	0.19	63.0	4.7	+7.8	9.9	Y95						3–2	20	2.81	49.28
		3–2	20	0.19	41.5	3.0	+10.6	9.2	S95									
		3–2	20	0.31	44.3	3.37	+10.4	9.8	K97									
		4–3	15	0.24	52.7	4.0	+9.9	9.0	Y95						4–3	15	3.55	63.02

Table 6 (continued).

IRAS	Star	Observations								Model								
		Line	HPBW "	rms (K)	I_{CO} (K km/s)	T_{MB} (K)	V_c (km/s)	V_e (km/s)	Ref	D (pc)	V_e (km/s)	dM/dt ($M_{\odot} \text{ yr}^{-1}$)	radius (cm) (")		Line	HPBW (")	T_{MB} (K)	I_{CO} (K km/s)
Region B (continued):																		
20213+0047	V865 Aql	2-1	25	0.03	—	—	—	—	BL94	840	(8.5)	$< 3.0 \cdot 10^{-7}$						
23595-1457	W Cet	1-0	23	0.19	—	—	—	—	H90	950	(8.5)	$< 3.4 \cdot 10^{-7}$						
		1-0	50	0.02	—	—	—	—	BL94									
		1-0	45	0.04	—	—	—	—	SL95									
		3-2	20	0.03	—	—	—	—	Y95									
Region C:																		
00213+3817	R And	1-0	45	—	3.71	—	-16	11	M90	490	9.3	$8.6 \cdot 10^{-7}$	$5.66 \cdot 10^{16}$	7.7	1-0	45	0.22	3.71
		1-0	50	0.04	5.73	0.44	-15.8	9.3	BL94						1-0	50	0.18	3.02
		2-1	25	0.05	6.5	0.73	-15.6	8.5	BL94						2-1	25	0.85	11.46
01159+7220	S Cas	1-0	23	0.36	—	0.44	-30.8	22.0	H90	860	20.0	$4.0 \cdot 10^{-6}$	$1.0 \cdot 10^{17}$	8.0	1-0	23	0.43	15.6
		1-0	45	—	3.43	—	-29	18	M90						1-0	45	0.12	4.29
		1-0	33	0.11	6.0	0.23	-26.0	19.0	N92						1-0	33	0.22	7.8
		1-0	50	0.03	4.63	0.14	-31.0	22.0	BL94						1-0	50	0.10	3.49
		2-1	25	0.03	8.1	0.29	-30.0	19.7	BL94						2-1	25	0.35	11.62
02143+4404	W And	1-0	33	0.09	4.5	0.43	-35.0	10.4	N92	630	8.5	$8.0 \cdot 10^{-7}$	$5.65 \cdot 10^{16}$	5.9	1-0	33	0.27	4.15
		1-0	50	0.02	1.37	0.12	-34.2	7.8	BL94						1-0	50	0.12	1.83
		2-1	25	0.01	3.0	0.29	-34.4	6.5	BL94						2-1	25	0.52	7.04
		3-2	20	0.08	7.0	0.59	-36.7	8.9	Y95						3-2	20	0.55	7.43
05374+3153	NO Aur	2-1	13	0.05	—	—	—	—	SL95	620	(8.5)	$< 1.1 \cdot 10^{-7}$						
		2-1	30	0.01	—	—	—	—	this work									
06331+1415	DY Gem	1-0	50	0.04	—	—	—	—	BL94	890	8.0	$2.4 \cdot 10^{-7}$	$2.87 \cdot 10^{16}$	2.1	1-0	50	0.01	0.18
		2-1	13	0.05	—	0.25	-16.0	8.0	SL95						2-1	13	0.25	3.50
06571+5524	R Lyn	1-0	50	0.01	0.32	0.03	+15.3	7.5	BL94	950	8.0	$3.5 \cdot 10^{-7}$	$3.51 \cdot 10^{16}$	2.5	1-0	50	0.017	0.27
		2-1	25	0.01	0.54	0.04	+16.6	7.7	BL94						2-1	25	0.092	1.25
		2-1	30	0.02	0.94	0.08	+15.7	9.3	this work						2-1	30	0.064	0.87

Table 6 (continued).

IRAS	Star	Observations								Model								
		Line	HPBW "	rms (K)	I_{CO} (K km/s)	T_{MB} (K)	V_c (km/s)	V_e (km/s)	Ref	D (pc)	V_e (km/s)	dM/dt ($M_{\odot} \text{ yr}^{-1}$)	radius $\frac{\text{cm}}{(\text{''})}$	Line	HPBW "	T_{MB} (K)	I_{CO} (K km/s)	
Region C (continued):																		
07043+2246	R Gem	1-0	23	0.10	—	0.65	-59.2	6.0	H90	850	5.4	$2.3 \cdot 10^{-7}$	$7.63 \cdot 10^{17}$	60.0	1-0	23	0.10	1.07
		2-1	13	0.12	—	1.40	-59.1	4.8	SL95						2-1	13	0.55	4.99
		3-2	20	0.07	1.7	0.28	-59.0	5.5	K97						3-2	20	0.18	1.57
07149+0111	RR Mon	1-0	45	0.01	—	—	—	—	SL95	1200	(8.5)	$< 7.0 \cdot 10^{-7}$						
07245+4605	Y Lyn	1-0	33	0.08	2.2	0.20	-0.7	8.6	N92	330	8.6	$2.3 \cdot 10^{-7}$	$2.73 \cdot 10^{16}$	5.5	1-0	33	0.14	2.50
09338-5349	UU Vel	1-0	45	0.11	—	—	—	—	SL95	1260	(8.5)	$< 4.0 \cdot 10^{-6}$						
13136-4426	UY Cen	2-1	23	0.02	—	0.07	-28.6	13.1	SL95	550	13.1	$2.1 \cdot 10^{-7}$	$2.36 \cdot 10^{16}$	2.9	2-1	23	0.07	1.67
		3-2	20	0.04	—	—	—	—	this work						3-2	20	0.18	1.57
16334-3107	ST Sco	1-0	50	0.02	0.61	0.06	-4.5	6.5	BL94	540	7.1	$1.2 \cdot 10^{-7}$	$1.98 \cdot 10^{16}$	2.5	1-0	50	0.01	0.15
		1-0	45	0.02	—	0.14	-1.2	7.3	SL95						1-0	45	0.01	0.19
		2-1	25	0.02	1.17	0.14	-5.8	7.6	BL94						2-1	25	0.09	1.24
17001-3651	RT Sco	1-0	45	0.02	—	0.20	-44.5	13.1	SL95	490	11.0	$4.6 \cdot 10^{-7}$	$3.7 \cdot 10^{16}$	5.0	1-0	45	0.06	1.36
		2-1	23	0.05	—	0.18	-44.4	9.6	SL95						2-1	23	0.31	5.92
17081+6422	TV Dra	1-0	50	0.02	0.13	0.03	+22.4	3.7	BL94	540	5.0	$4.6 \cdot 10^{-8}$	$1.34 \cdot 10^{16}$	1.6	1-0	50	0.003	0.034
		2-1	13	0.04	1.0	0.15	+22	6	O93						2-1	13	0.17	1.67
		2-1	25	0.01	0.40	0.05	+21.1	5.0	BL94						2-1	25	0.05	0.46
		2-1	13	0.09	—	0.30	+21.2	5.1	SL95									
18575-0139	VX Aql	1-0	45	0.12	—	—	—	—	SL95	1400	7.8	$3.2 \cdot 10^{-7}$	$3.41 \cdot 10^{16}$	1.6	1-0	45	0.01	0.15
		2-1	23	0.01	—	0.05	+6.7	7.8	SL95						2-1	23	0.05	0.67
18586-1249	ST Sgr	1-0	50	0.01	0.42	0.03	+54.6	9.3	BL94	670	10.0	$3.5 \cdot 10^{-7}$	$3.25 \cdot 10^{16}$	3.2	1-0	50	0.022	0.04
		1-0	45	0.01	—	0.06	+55.1	9.6	SL95						1-0	45	0.027	0.54
		2-1	25	0.04	—	—	—	—	BL94						2-1	25	0.12	2.06
		2-1	23	0.03	—	0.11	+49.8	11.2	SL95						2-1	23	0.14	2.53
19111+2555	S Lyr	2-1	13	0.04	—	0.40	+51.2	13.9	SL95	1500	13.9	$2.1 \cdot 10^{-6}$	$8.10 \cdot 10^{16}$	3.6	2-1	13	0.40	9.0

Table 6 (continued).

IRAS	Star	Observations								Model												
		Line	HPBW	rms	I_{CO}	T_{MB}	V_c	V_e	Ref	D	V_e	dM/dt	radius		Line	HPBW	T_{MB}	I_{CO}				
		"	(K)	(K km/s)	(K)	(km/s)	(km/s)		(pc)	(km/s)	($M_{\odot} \text{ yr}^{-1}$)	(cm)	(")	(")	(")	(K)	(K km/s)					
Region C (continued):																						
19126–0708	W Aql	1–0	23	0.09	–	2.31	–24.6	19.3	H90	610	18.7	$1.3 \cdot 10^{-5}$	$2.12 \cdot 10^{17}$	23.2	1–0	23	2.98	102.4				
		1–0	45	–	26.2	–	–25	20	M90													
		1–0	45	0.05	28.4	0.96	–24.0	18.1	N92										1–0	45	1.14	35.54
		1–0	50	0.03	27.7	0.98	–24.0	17.7	BL94										1–0	50	0.95	29.5
		1–0	45	0.22	–	1.30	–24.1	18.3	SL95													
		2–1	25	0.04	43.1	1.60	–24.1	17.4	BL94										2–1	25	26.7	78.2
		2–1	30	0.03	54.8	2.10	–25.2	19.3	K97										2–1	30	1.96	56.98
		2–1	13	0.16	–	6.05	–24.0	18.8	SL95										2–1	13	6.98	217.3
		2–1	23	0.25	–	2.04	–24.3	18.0	SL95										2–1	23	3.05	90.0
		3–2	20	0.10	93.2	3.51	–23.8	19.6	K97					3–2	20	2.70	76.95					
19133–1703	T Sgr	1–0	50	0.02	–	–	–	–	BL94													
		1–0	45	0.02	–	–	–	–	SL95													
		2–1	25	0.04	–	–	–	–	BL94													
		2–1	23	0.02	–	0.06	+10.8	14.1	SL95	810	14.1	$4.0 \cdot 10^{-7}$	$3.22 \cdot 10^{16}$	2.7	2–1	23	0.06	1.53				
19354+5005	R Cyg	1–0	50	0.01	2.52	0.15	–17.5	9.9	BL94	900	10.5	$1.7 \cdot 10^{-6}$	$8.16 \cdot 10^{16}$	6.1	1–0	50	0.11	2.0				
		2–1	25	0.02	5.04	0.33	–17.2	11.4	BL94										2–1	25	0.43	7.06
		3–2	20	0.17	14.6	1.3	–18.2	10.4	S95										3–2	20	0.44	7.18
22036+3315	RZ Peg	2–1	13	0.04	–	0.21	–23.4	12.6	SL95	1560	12.6	$1.1 \cdot 10^{-6}$	$5.93 \cdot 10^{16}$	2.5	2–1	13	0.21	4.57				
*22196–4612	π^1 Gru	1–0	45	0.05	6.9	0.33	–13.2	19.4	N92	160	11.0	$4.6 \cdot 10^{-7}$	$3.70 \cdot 10^{16}$	15.5	1–0	45	0.53	11.80				
		1–0	45	0.08	–	0.60	–	–	SL95													
		2–1	23	–	–	2.20	–12.5	11.0	S92										2–1	23	2.20	45.67
		2–1	23	0.06	–	2.00	–	–	SL95													
23554+5612	WY Cas	2–1	13	0.04	–	0.50	+7.5	13.3	SL95	1300	13.3	$1.8 \cdot 10^{-6}$	$7.65 \cdot 10^{16}$	3.9	2–1	13	0.50	1.08				

Table 6 (continued).

IRAS	Star	Observations								Model								
		Line	HPBW	rms	I_{CO}	T_{MB}	V_c	V_e	Ref	D	V_e	dM/dt	radius		Line	HPBW	T_{MB}	I_{CO}
		"	(K)	(K km/s)	(K)	(km/s)	(km/s)		(pc)	(km/s)	($M_{\odot} \text{ yr}^{-1}$)	(cm)	(")	(")	(K)	(K km/s)		
Region D:																		
00578+5620	V365 Cas	1-0	50	0.01	—	—	—	—	BL94	800	7.2	$7.0 \cdot 10^{-8}$	$1.53 \cdot 10^{16}$	1.3	2-1	13	0.07	0.98
		2-1	25	0.03	—	—	—	—	BL94									
		2-1	13	0.02	—	0.07	-2.1	7.2	SL95									
04352+6602	T Cam	1-0	50	0.02	—	—	—	—	BL94	520	(8.5)	$< 2.2 \cdot 10^{-7}$						
		2-1	25	0.05	—	—	—	—	BL94									
04543+4829	TV Aur	1-0	50	0.02	—	—	—	—	BL94	780	(8.5)	$< 2.6 \cdot 10^{-7}$						
		2-1	25	0.03	—	—	—	—	BL94									
07095+6853	AA Cam	2-1	13	0.02	—	0.06	-43.5	17.9	SL95	880	17.9	$2.9 \cdot 10^{-7}$	$2.67 \cdot 10^{16}$	2.0	2-1	13	0.06	2.14
07399-1045	SU Mon	1-0	50	0.01	—	—	—	—	BL94	780	(8.5)	$< 2.6 \cdot 10^{-7}$						
		1-0	45	0.01	—	—	—	—	SL95									
		2-1	25	0.03	—	—	—	—	BL94									
12417+6121	S UMa	2-1	30	0.01	—	—	—	—	this work	1650	(8.5)	$< 4.8 \cdot 10^{-7}$						
*13440-5306	AM Cen	1-0	45	0.02	—	0.08	-27.4	5.4	SL95	910	5.4	$3.5 \cdot 10^{-7}$	$4.13 \cdot 10^{16}$	3.0	1-0	45	0.054	0.55
		2-1	23	0.04	—	0.20	—	—	SL95						2-1	23	0.27	2.33
13477-6009	VX Cen	1-0	45	0.03	—	—	—	—	SL95	530	(8.5)	$< 4.6 \cdot 10^{-7}$						
17206-2826	V521 Oph	1-0	50	0.01	—	—	—	—	BL94	580	(8.5)	$< 2.5 \cdot 10^{-7}$						
		1-0	45	0.01	—	—	—	—	SL95									
19311+2332	EP Vul	1-0	50	0.02	0.94	0.12	-0.2	5.2	BL94	650	5.4	$2.9 \cdot 10^{-7}$	$3.70 \cdot 10^{16}$	3.8	1-0	50	0.07	0.68
		1-0	45	0.01	—	0.08	-0.7	5.6	SL95						1-0	45	0.08	0.84
		2-1	25	0.02	1.56	0.20	+0.1	5.5	BL94						2-1	25	0.34	2.99
		2-1	13	0.14	—	0.52	-0.1	4.7	SL95									
20026+3640	AA Cyg	1-0	50	0.03	1.51	0.11	+22.7	9.4	BL94	550	7.1	$3.1 \cdot 10^{-7}$	$3.46 \cdot 10^{16}$	4.2	1-0	50	0.06	0.80
		2-1	13	0.13	—	0.95	+27.9	4.8	SL95						2-1	13	1.05	12.82
22476+4047	RX Lac	1-0	45	0.13	—	—	—	—	SL95	380	3.4	$4.0 \cdot 10^{-8}$	$1.4 \cdot 10^{16}$	4.1	2-1	13	0.67	4.42
		2-1	13	0.12	—	0.68	-15.4	3.4	SL95									

Table 6 (continued).

IRAS	Star	Observations								Model								
		Line	HPBW	rms	I_{CO}	T_{MB}	V_c	V_e	Ref	D	V_e	dM/dt	radius		Line	HPBW	T_{MB}	I_{CO}
		"	(K)	(K km/s)	(K)	(km/s)	(km/s)		(pc)	(km/s)	($M_{\odot} \text{ yr}^{-1}$)	(cm)	(")	(")	(")	(K)	(K km/s)	
04123+2357	GCGSS89	2-1	30	0.02	-	-	-	-	this work	650	(8.5)	$< 1.7 \cdot 10^{-7}$						
04497+1410	ρ^1 Ori	1-0	45	0.02	-	-	-	-	SL95	330	(8.5)	$< 2.0 \cdot 10^{-7}$						
04599+1514	GP Ori	3-2	20	0.04	-	-	-	-	this work	1100	(8.5)	$< 5.2 \cdot 10^{-7}$						
*06197+0327	FU Mon	2-1	30	0.01	0.66	0.16	-41.7	2.8	this work	860	2.8	$1.0 \cdot 10^{-7}$	$7.70 \cdot 10^{17}$	59.8	2-1	30	0.14	0.63
07507-1129	NQ Pup	3-2	20	0.04	-	-	-	-	this work	1160	(8.5)	$< 6.3 \cdot 10^{-7}$						
13163-6031	TT Cen	1-0	45	0.04	-	0.05	+5.2	24.0	SL95	1070	24.7	$4.6 \cdot 10^{-6}$	$1.0 \cdot 10^{17}$	6.2	1-0	45	0.06	2.67
		2-1	23	0.05	-	0.24	+5.5	25.4	SL95						2-1	23	0.21	8.92
20044+2417	DK Vul	1-0	50	0.02	1.33	0.04	-13.9	8.9	BL94	910	5.0	$2.9 \cdot 10^{-7}$	$3.83 \cdot 10^{16}$	2.8	1-0	50	0.04	0.38
		2-1	25	0.02	1.41	0.21	-14.2	5.3	BL94						2-1	25	0.20	1.64
		2-1	13	0.05	-	1.10	-14.2	4.7	SL95						2-1	13	0.74	5.93
20100-6225	GCGSS1195	1-0	45	0.04	-	-	-	-	SL95	900	(8.5)	$< 1.0 \cdot 10^{-6}$						
		2-1	23	0.14	-	-	-	-	SL95									
20120-4433	RZ Sgr	1-0	45	0.03	-	0.36	-31.6	14	SL95	820	8.8	$2.1 \cdot 10^{-6}$	$9.90 \cdot 10^{16}$	8.1	1-0	45	0.30	4.36
		2-1	23	0.04	-	0.98	-31.2	8.8	SL95						2-1	23	1.08	14.6

References:

H90: Heske 1990; M90: Margulis et al 1990; S92: Sahai 1992; N92: Nyman et al. 1992; N93: Nyman et al. 1993; O93: Omont et al. 1993; KJ94: Kahane & Jura 1994; BL94: Bieging & Latter 1994; SL95: Sahai & Liehti 1995; Y95: Young 1995; S95: Stanek et al. 1995; K97: Knapp et al. 1997b

Notes:

- 06197+0327, FU Mon: Data from Sahai & Liehti (1995) not used – see text;
- 09076+3110, RS Cnc: CO(2-1) line profile has two components – see text;
- 13440-5306, AM Cen: Values for central velocity V_c and outflow velocity V_e given by SL95 are averages of the values for the CO(1-0) and CO(2-1) lines;
- 22196-4612, π^1 Gru: SL95 do not list values for V_c and V_e because of the line wings

This article was processed by the author using Springer-Verlag
L^AT_EX A&A style file *L-AA* version 3.